SPEED-UPS AND SLOWDOWNS: INSIGHTS INTO VELOCITY VARIATIONS MEASURED FROM 2009-2011 ON YAHTSE GLACIER, ALASKA

By

Jessica Zimmerman Mejia, B.S.

A Thesis Submitted in Partial Fulfillment of the Requirements

for the Degree of

Master of Science

in

Geophysics

University of Alaska Fairbanks

December 2016

APPROVED:

Christopher F. Larsen, Committee Chair
Martin Truffer, Committee Member
Carl Tape, Committee Member
Paul McCarthy, Chair
Department of Geosciences
Paul Layer, Dean
College of Natural Science and Mathematics
Michael Castellini, *Dean of the Graduate School*

Abstract

Water at the bed of a glacier can alter the basal stress distribution that governs basal motion and is responsible for short-term velocity variations. Accelerated basal motion has lead to increased ice discharge on tidewater glaciers, influencing the glacial contribution to sea level rise. The development of a temporally high-resolution model requires understanding the dynamic elements of the subglacial drainage system that govern short-term velocity variations. Here, we use global positioning system (GPS) observations to document the relationship between basal motion and widely variable water inputs on Yahtse Glacier over three years. Yahtse Glacier is a temperate, grounded, tidewater glacier terminating in Icy Bay, southcentral Alaska. We simultaneously measured surface ice velocity along the glacier's centerline using high-resolution GPS stations, weather data and glaciohydraulic tremor amplitude from 11 June 2009 through 11 September 2011. Yahtse exhibits a repeated summer slowdown facilitated by speed-up events and winter speed-up that ends in mid-winter when ice velocities return to pre-melt-season values. We find that the extent of the summer slowdown is determined by the presence of late-summer heavy rainfall that triggers speed-up events coupled with extra slowdowns. The summer minimum speed impacts flow speeds until mid-winter, therefore controlling average annual ice velocities. Measurements of glaciohydraulic tremor and surface uplift indicate extra slowdowns are the result of the release of subglacially stored water and the dynamic response of the isolated cavity system. We apply the basal hydrology model developed by Bartholomaus [Journal of Glaciology, **57**, 206 (2011)] and adapted by Brinkerhoff [Annals of Glaciology, **57**, 72 (2016)] to the ablation area of Yahtse Glacier. The model reproduces a majority of the transient speed-up events observed, but not the associated extra slowdowns or the season trend of a summer slowdown and winter speed-up. For the model to reproduce the short lived extra slowdowns and subsequent seasonal velocity trends, we suggest the model may need to account for the isolated subglacial cavity system.

Table of Contents

Page

Title Page . . . . . **i**

Abstract . . . . . **iii**

Table of Contents . . . . . **v**

List of Figures . . . . . **vii**

List of Tables . . . . . **ix**

Acknowledgements . . . . . **xi**

Chapter 1 Introduction **1**

Chapter 2 Methods **5**

2.1 Study Area 5

2.2 Measurements 5

2.2.1 GPS Data 5

2.2.2 Weather Data 8

2.3 Data Analysis 10

2.3.1 GPS Data 10

2.3.2 Water Input Model 13

2.3.3 Glaciohydraulic Tremor 15

2.3.4 Basal Hydrology Model 16

Chapter 3 Results **21**

3.1 Horizontal Ice Motion 23

3.1.1 Seasonal Flow Characteristics 23

3.1.2 Speed-Up Events 23

3.1.3 Extra Slowdowns 24

3.2 Vertical Ice Motion 25

3.3 Glaciohydraulic Tremor 26

3.4 Basal Hydrology Model 27

Chapter 4 Discussion **31**

4.1 Glacier Flow on Seasonal Timescales 31

4.1.1 Summer Slowdown 33

4.1.2 Winter Speed-Up 34

4.1.3 Controls on Glacier Flow 35

4.2 Speed-Up Events 36

4.3 Extra Slowdowns 39

4.3.1 Extra Slowdowns and Storage 39

Page

4.3.2 Extra Slowdowns and the Isolated Cavity System 41
4.4 Basal Hydrology Model 44
Chapter 5 Conclusion 47
Chapter 6 References 49

List of Figures

Page

2.1 Map of Yahtse Glacier, AK 6
2.2 GPS Station at the End of the 2009 Melt-Season 7
2.3 Yahtse, Yakutat and Bering Weather Comparison 9

3.1 2009–2011 Timeseries dataset 22
3.2 2009 Vertical Motion 26
3.3 Basal Hydrology Model Results 29

4.1 Comparison of Annual Ice Velocities 32
4.2 Comparison of Annual Cumulative Water Input 36
4.3 Speed-up Event and Water Input Rate Correlation 37
4.4 Speed-up Event Sensitivity 38
4.5 SE3–5 Timing 40
4.6 SE21 Timing 41
4.7 2009 Uplift Timeseries 42
4.8 Comparison Between Uplift and Uplift Rate for SE3–5 44

List of Tables

Page

2.1 Instrument Activity 8
2.2 Basal Hydrology Model Parameters 19

Acknowledgements

Foremost, I would like to thank my thesis advisor, Chris Larsen, for giving me this opportunity and for his patience, guidance, and helpful advise. I am grateful for the freedom I was given to choose the direction of this research and thankful for the critical feedback that helped me shape and clarify my ideas. Thank you for giving me the opportunity to participate in your research and see Yahtse Glacier in person. I would also like to thank my committee members, Martin Truffer and Carl Tape, for their time, insightful comments, and hard questions. Special thanks to Timothy Bartholomaus for his previous work on Yahtse and for being available to provide valuable comments throughout this project. My time at UAF wouldn't have been the same without being a part of the Glaciers Group, thank you to everyone for sharing your knowledge, and for your generous support, friendship, and assistance.

Thanks to my family for their unwavering support and encouragement. I must express my very profound gratitude to my spouse Jorge Mejia for moving to Alaska with me and for his love, energy, curiosity, and friendship. Finally, I would like to dedicate this thesis to my grandfather, Anthony Krawec, the wisest and kindest person I have ever known. Our conversations stimulated my curiosity for science and put me on the path to where I am today.

Chapter 1
Introduction

Climate change and associated sea level rise are among the biggest issues facing the global community. Glaciological models that calculate sea level rise projections need additional improvements to further constrain the upper bounds of the projections. To improve these models a detailed understanding of the physics that control glacial behavior on sub-weekly timescales is necessary. Accelerated basal motion results in increased ice discharge at the terminus of tidewater glaciers, thereby influencing sea level rise (Rignot and Kanagaratnam, 2006; O'Neel et al., 2005). At this time, ice sheet models do not consider hydrologic transience or successfully span the range of sub-seasonal timescales over which velocity varies dramatically (Bartholomaus et al., 2007; Willis, 1995). The development of a temporally high-resolution model requires understanding the dynamic elements of the subglacial drainage system that govern short-term velocity variations. This thesis addresses the following research questions to understand the relationship between water input and basal motion from three years of measurements of Yahtse Glacier, a tidewater glacier in southcentral Alaska.

1. How much does water input contribute to the velocity variations observed on Yahtse?
2. Does the glacier's response to water input change over time?
3. Does the glacier exhibit the same ice velocities from year to year?
4. Is the winter velocity inversely related to meltwater input (Burgess et al., 2013a)?
5. Can we predict the ice velocities based on the velocity record from the previous year?

The presence of water at the bed of a glacier can affect surface ice velocities by altering the basal stress distribution that governs basal motion (Fountain and Walder, 1998). Basal motion involves the sliding of ice over the bed and deformation of basal till, both of which are sensitive to water and can vary on short timescales (Truffer et al., 2001). A relationship between water input, from surface melt or rainfall, and increased ice-flow speed has been established through observations of short-duration velocity variations of temperate and polythermal glaciers (Anderson et al., 2004; Iken and Bindschalder, 1986; Meier et al., 1994; Sugiyama and Gudmundsson, 2003; Copland et al., 2003), ice caps (Wyatt and Sharp, 2015), and the Greenland Ice Sheet (Zwally et al., 2002; Bartholomew et al., 2012; Sundal et al., 2011). Transient velocity variations have been attributed to increased pressurization of the subglacial drainage system, separation from the bed, loss of basal traction, till dilation, variable water storage, the transient evolution of the subglacial drainage system and shifts in the glacier's stress field (Howat et al., 2008). Despite the relationship between basal motion and the configuration of the subglacial drainage network, neither measured subglacial

water pressure nor the volume of water in storage can entirely explain observed variations in basal motion, illustrating the need for further investigation (Bindschadler, 1983; Bartholomaus et al., 2007).

Water is transported to the bed through a dynamic network of conduits that are formed by water flowing along the bottom of crevasses and entering preexisting veins or microfractures (Fountain and Walder, 1998). These conduits are sustained by melt enlargement from the energy dissipated by flowing water. If the flux of water decreases, the inward creep of ice will act to close the conduits (Fountain and Walder, 1998). Upon reaching the bed, runoff enters a complex subglacial drainage network before emerging at the terminus.

Water flows along the bed in one or both of two distinct flow arrangements known as the fast and slow drainage systems, a partitioning which describes the water discharge response to input variations (Raymond et al., 1995). The slow drainage system covers a large fraction of the bed, draining water through linked cavities and canals incised into rock and/or subglacial sediment till. Cavities form on the lee side of bed-rock bumps, increasing in size with increasing basal motion (Fountain and Walder, 1998). The slow drainage system can be composed of coexisting linked and isolated cavities (Weertman, 1964). Isolated cavities increase in size and pressure, as long as the pressure is less than overburden pressure, as they collect basal and internal meltwater. The isolated cavities can occasionally connect with the subglacial drainage system to varying extents (Lliboutry, 1979). As more isolated cavities connect to the subglacial drainage system, a change in water pressure has a greater control on sliding velocity (Iken and Truffer, 1997).

The fast drainage system is composed of Röthlisberger channels, or R channels, which have a semicircular cross section and are incised into the basal ice (Röthlisberger, 1972). This fast drainage system is characterized by a low surface-to-volume ratio covering a small fraction of the bed and a higher basal friction coefficient (Kamb and Echelmeyer, 1986). R channels are formed when the englacial water flux is great enough to cause a pressure perturbation that will enlarge cavity orifices unstably and spawn the R channel system (Kamb, 1987). The R channels are then sustained by a balance between widening of the channel walls through heat dissipation of water flow, and narrow by the inward creep of ice (Fountain and Walder, 1998). Water flows through a channelized system at low pressures, therefore water in the high pressure linked-cavity system will drain towards the channels.

Glacier flow velocities vary over a wide range of timescales (Meier and Post, 1987). Spring speed-up has been observed on many glaciers and is interpreted as a response to the initial disruption of the winter subglacial drainage system by the influx of meltwater (Hubbard and Nienow, 1997). While seasonal velocity variations are a common feature, velocity is known to vary on a wide range of shorter timescales. Shorter-period velocity variations, on timescales on the order of

hours to weeks, have been observed on a number of glaciers (e.g. Willis, 1995). Ice velocities can respond more to short-term water inputs than to changes in mean water flow (Schoof, 2010).

We use global positioning system (GPS) observations to document the relationship between basal motion and widely variable water inputs on Yahtse Glacier from 11 June 2009 through 11 September 2011. Simultaneous measurements of surface ice velocities in the ablation and accumulation areas, weather data, and glaciohydraulic tremor amplitude were compared through three melt-seasons and two winters to infer the basal processes governing basal motion. Yahtse exhibits seasonal velocity variations consisting of a summer slowdown from May through early September. This is followed by a winter speed-up beginning in October, ending in mid-winter when ice velocities return to pre-melt-season values. These seasonal patterns are governed by water inputs. We find that the extent of the summer slowdown is determined by the presence of late-summer heavy rainfall that triggers speed-up events coupled with extra slowdowns. The summer minimum speed impacts flow speeds until mid-winter, controlling average annual ice velocities. Measurements of glaciohydraulic tremor and surface uplift suggest extra slowdowns are the result of the release of subglacially stored water and the dynamic response of the isolated cavity system. We apply the basal hydrology model developed by Bartholomaus and others (2011) and adapted by Brinkerhoff and others (2016) to the lower 15 km of Yahtse Glacier. The model reproduces a majority of the transient speed-up events, but not the associated extra slowdowns or the season trend of a summer slowdown and winter speed-up. For the model to reproduce the short lived extra slowdowns and the seasonal velocity trends, we suggest the model may need to account for the isolated subglacial cavity system.

Chapter 2
Methods

2.1 Study Area

Yahtse Glacier is a 63 km long temperate, tidewater glacier located in southcentral Alaska covering an area of 1018 km^2 (Figure 2.1). The Barkley Ridge and the Saint Elias Mountains mark the northern boundary of Yahtse, separating it from the Bagley Ice Field. Yahtse is the largest of four temperate tidewater glaciers that terminate into Icy Bay, Alaska. During the Little Ice Age in the 19th century these glaciers reached their most recent maximum extent, completely filling what is now Icy Bay and terminating into the Gulf of Alaska. Following the end of the Little Ice Age, these glaciers began to retreat with rates as high as 400 meters per year. In 1990, after undergoing 40 km of retreat (Barclay et al., 2009), Yahtse was the first glacier in Icy Bay to complete the retreat phase of the tidewater glacier cycle (Post, 1971), and began to re-advance. Yahtse has since advanced 2 km as of September 2011 and continues to advance approximately 100 meters per year on top of the large seasonal variations. A seasonal pattern of spring advance and fall retreat ranging over approximately 300 m has been observed as a sub-cycle within the multi-year advance (Bartholomaus et al., 2012).

The accumulation area is a broad, low gradient upper basin extending 45 km and decreasing in elevation from 1400–900 m. The transition from the accumulation area to the ablation area occurs within an 8 km long section where the slope steepens and the glacier loses approximately 300 m elevation. The next 5 km downglacier is low-gradient and is marked by increased crevassing as ice flows around Guyot Hill (Figure 2.1). Yahtse then drains through an icefall (1% of glacier area) in which the ice surface drops 700 m in elevation over 5 km before terminating into Icy Bay (Bartholomaus, 2014). Laser altimetry of the glacier's longitudinal profile together with water depth soundings taken 1.5 km from the terminus indicate that Yahtse's centerline ice thickness at the calving face is approximately 170 m, with the fjord being no deeper than 110 m. The ice thickness is well above the flotation limit for water depths (< 140 m), and therefore the terminus is grounded throughout the year (Bartholomaus, 2014).

2.2 Measurements

2.2.1 GPS Data

Several on-ice GPS stations, bedrock seismic stations and a weather station were deployed during the first field campaign in June 2009 to investigate the temporal and spatial relationships between ice motion and basal processes of Yahtse Glacier. Each GPS station was equipped with a Trimble 5700 receiver and a Trimble Zephyr antenna that recorded in 15-second intervals. The stations were expected to run with autonomous lifespans of approximately 200 days. We returned

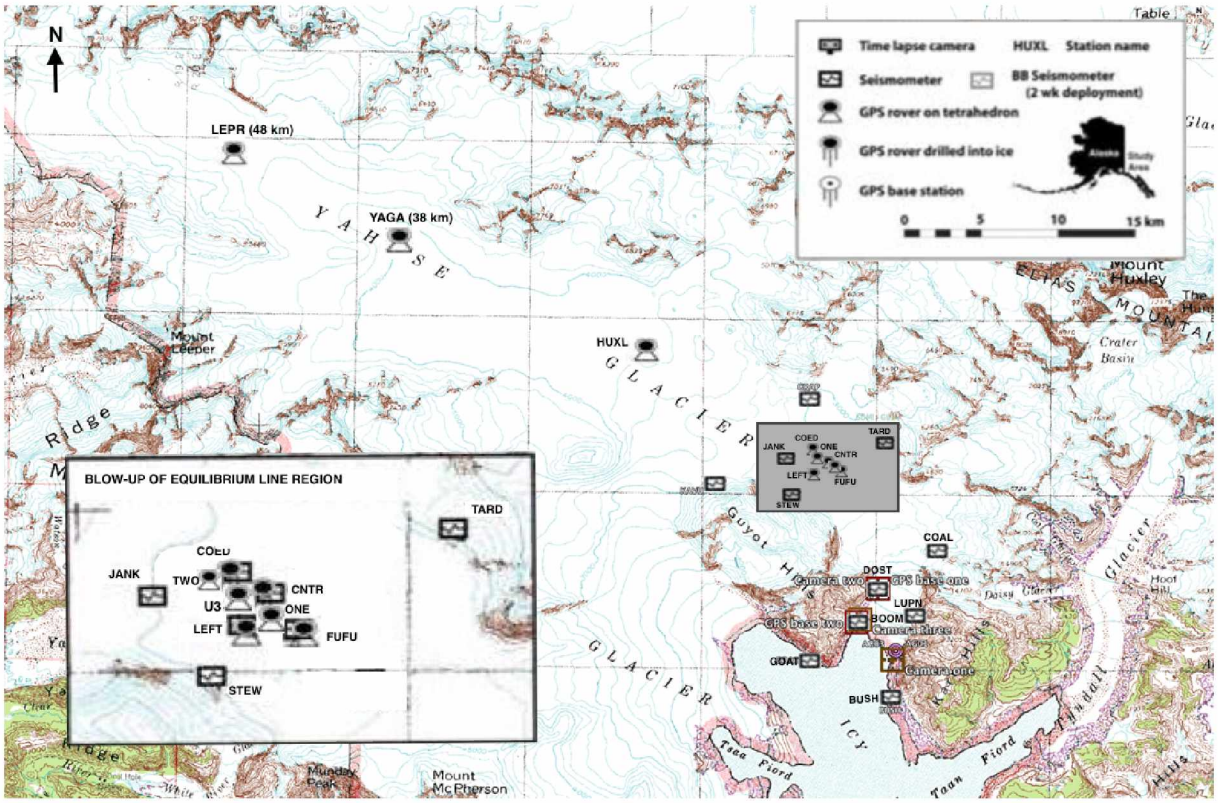

Figure 2.1. Map of Yahtse Glacier, AK. Instrumentation is depicted in the initial position with a zoom-in of the main cluster of GPS (permanent and temporary) stations and seismic stations in Yathse's ablation area.

to Yahtse at the beginning and end of each melt-season to service the GPS stations. In the ablation area 11 km, 12 km, and 14 km from the terminus we initially deployed three GPS stations (CNTR, COED, LEFT) along the glacier's center line. In the accumulation area approximately 25 km, 42 km, and 52 km from the terminus we deployed an additional three GPS stations (HUXL, YAGA, LEPR) along the glacier's centerline (Figure 2.1). The names of GPS stations and the dates they were actively recording throughout the study are displayed in Table 2.1.

Two of the GPS stations (CNTR and COED) in the ablation area had the antenna poles drilled into the ice in order to record positions throughout the melt-season and winter. We attached antennas to platforms supported by three steel poles drilled 10–12 m into the ice. The distance between the ice surface and antenna increases as ice ablates (Figure 2.2). Anticipating this separation we attached the receiver and power system to a self-lowering anchor so they float on the ice surface. The receiver and power system were buried in snow over the winter but the height of the antenna allowed for continued recording.

GPS station LEFT in the ablation area, as well as the three stations distributed along the centerline in the accumulation area were attached to tetrahedra and placed on the snow-covered surface

Figure 2.2. GPS Station at the End of the 2009 Melt-Season. Station CNTR is located in the ablation area where the antenna poles are drilled into ice. This photo was taken on the return trip to Yahtse Glacier, AK at the end of the 2009 melt-season.

of Yahtse. Consequently, the data record of these stations was affected by melt and surface lowering throughout the season. These stations were retrieved at the end of the melt-season on the return trip to Yahtse in September 2009.

Return trips to Yahtse were made twice a year at the beginning and end of the melt-season in 2010 and 2011. Early season trips involved collecting recorded data, maintenance and deploying additional temporary GPS stations. During the second return trip of 2010 the two permanent stations (CNTR and COED) were relocated up-glacier to the GPS coordinates recorded when first deployed in early 2009. The relocation of GPS stations allows us to more accurately compare GPS measurements from different years as the station will traverse the same path along the glacier each year.

From this field study, we have obtained three years of GPS data with one period of missing data from 20 January 2010 to 21 May 2010. A return trip to Yahtse was made on 21 May 2010 where two temporary GPS stations on tetrahedra (FUFU and U3) were deployed and stations HUXL and LEPR in the accumulation area were serviced. The temporary stations were retrieved and stations CNTR and COED serviced on the end of season return trip on 10 September 2011.

Our main station CNTR recorded throughout the winter. We deployed two additional temporary GPS stations (ONE and TWO) and serviced station YAGA in the accumulation area on 12 April 2011. These two temporary stations (ONE and TWO) recorded until our final return trip to Yahtse on 11 September 2011.

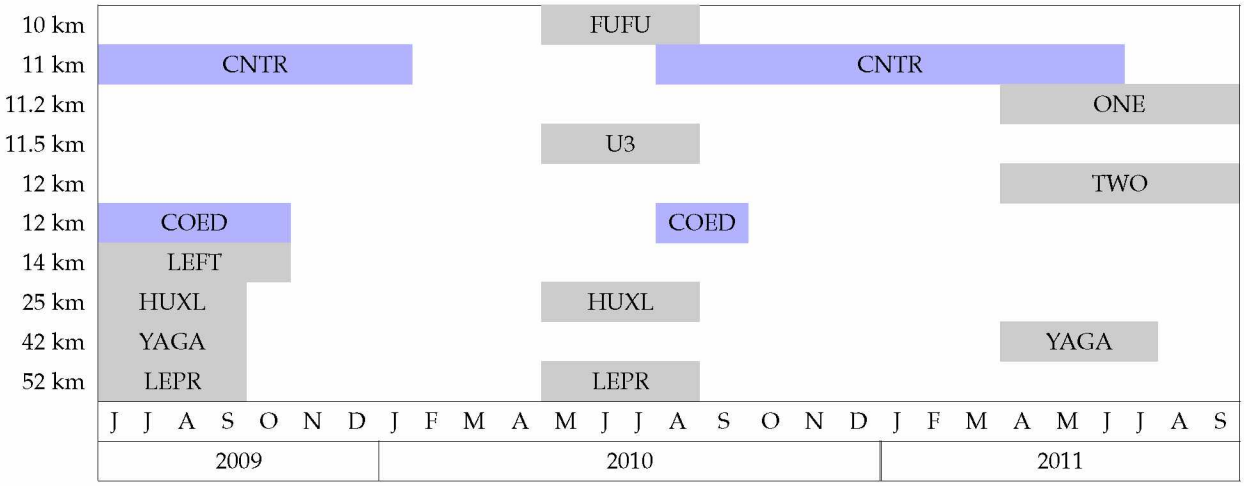

Table 2.1. Instrument Activity. Each row represents the months each GPS station was actively recording throughout the study. The numbers on the left correspond to each station's distance from the terminus. The blue boxes represent the permanent GPS stations drilled into the ice and gray boxes represent temporary GPS stations on tetrahedra.

2.2.2 Weather Data

Weather data were collected by deploying a weather station near Yahtse's terminus at the location of camp on the east side of the fjord. The weather station was equipped with a HOBO U30 NRC data logger, a temperature/RH smart sensor with a solar radiation shield, and a Davis rain gauge. The rain gauge measured rainfall using a tipping bucket with a magnetic reed switch that pivots on a metal shaft. This instrument has a measurement range of a maximum of 4000 tips per logger interval or 10.2 cm per hour, an accuracy of $\pm 4\%$ and a 214 cm^2 collection area. The weather station was deployed from 14 June 2009 to 11 September 2011, recording measurements every five minutes.

We determined the weather data recorded at Yahtse Glacier was accurate through comparison of daily air temperatures and precipitation measurements from two simultaneously recording weather stations located in Yakutat, AK and near the terminus of Bering Glacier, AK. The National Oceanic and Atmospheric Administration (NOAA) operates a continuously recording weather station located at the Yakutat Airport, approximately 120 km west of Yahtse (Menne et al., 2012). This weather station is equipped with an Automated Surface Observing System (ASOS) Hygro-Thermometer that has a maximum error of $\pm 1°C$, and an All Weather Precipitation Accumulation

Gauge (AWPAG) which uses an automated weighing gauge with an accuracy of ±4%. Weather data from Bering Glacier was measured by the Western Regional Climate Center's Remote Automatic Weather Station (2015) located near the terminus of Bering Glacier, approximately 120 km west of Yahtse. This weather station was equipped with a similar thermometer and tipping bucket rain gauge used on Yahtse.

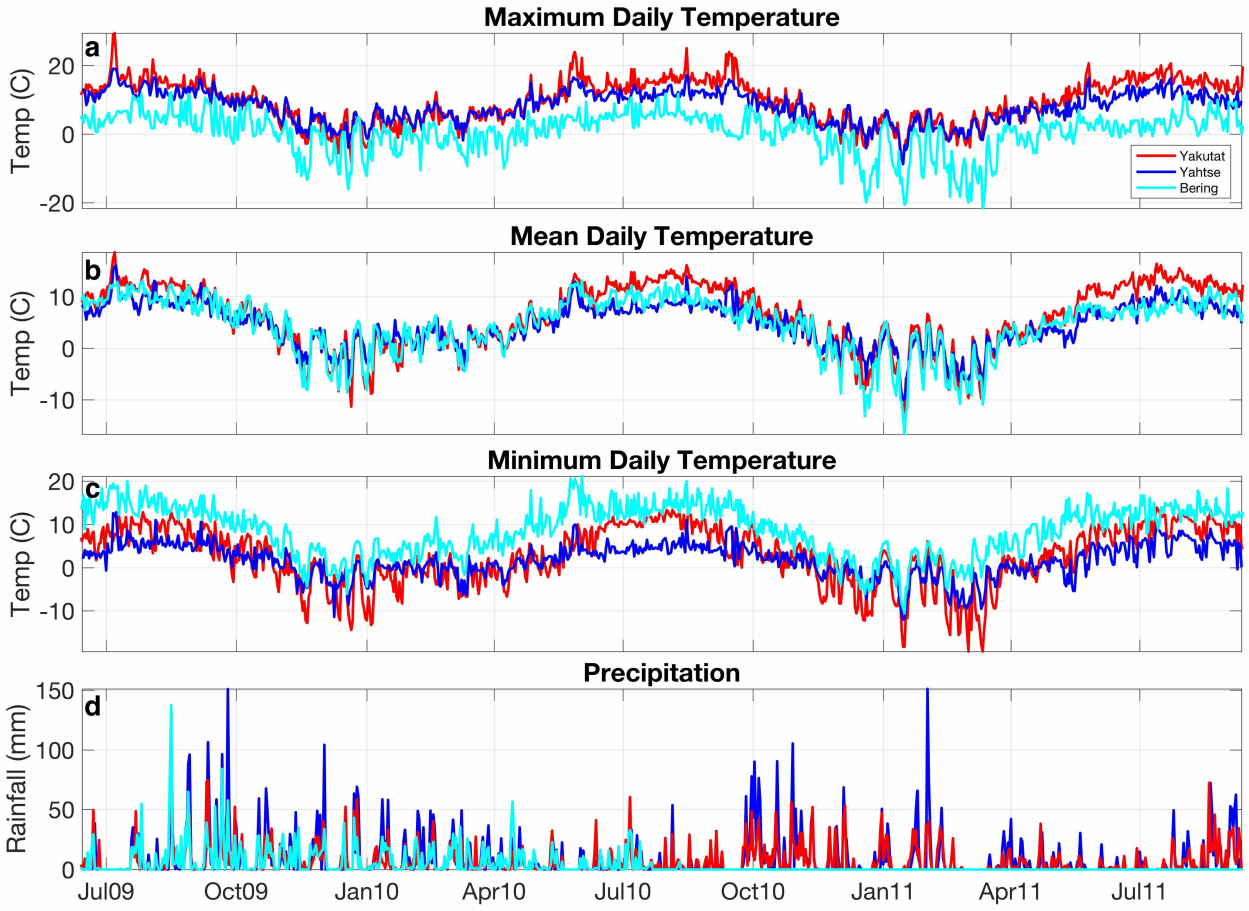

Figure 2.3. Yahtse, Yakutat and Bering Weather Comparison. A comparison of daily weather between data collected from our weather staton at the terminus of Yahtse Glacier (Blue), a NOAA weather station in Yakutat, AK (Red) and a WRCC weather station located on ice at Bering Glacier, AK (Cyan). (a) Maximum daily temperature (b) Mean daily temperature (c) Minimum daily temperature (d) Total daily rainfall

A comparison of daily temperatures (Figure 2.3a–c) revealed a good agreement between air temperatures and no large scale errors at our weather station at Yahtse Glacier. There is a good correlation between temperatures at Yahtse and Yakutat, with Yakutat showing consistently higher summer temperatures than those recorded at Yahtse. The daily precipitation (Figure 2.3d) record shows rain events recorded at each location with Yahtse receiving more precipitation on average than Yakutat. We expect to see more precipitation at Yahtse due to the effects of orographic precip-

itation associated with cooling air and updrafts over the mountains can lead to increased moisture (Roe, 2005). We also expect to see cooler temperatures during the summer due to the generation of katabatic winds which act to lower temperatures, especially in midsummer when more ice is exposed (van den Broeke, 1997). This comparison shows good agreement between the timing of the rain events recorded at Yahtse Glacier and shows no evidence of large scale errors in rainfall measurements.

The air temperature sensor at the terminus was damaged by a bear on 8 May 2011. To fill in the missing temperature data we retrieved complete weather data from the NOAA weather station located at Yakutat Airport. Yakutat had consistently higher magnitude which we adjusted for by calculating the mean of the three year timeseries of mean daily temperatures for each location. This resulted in Yakutat having a mean summer temperature 4.3°C greater than Yahtse, we use this value to adjust the Yakutat temperatures from 8 May–11 September 2011.

To calculate the elevation dependent air temperature to extrapolate measurements from the terminus we recorded temperatures in the accumulation area in the summer of 2010. On-ice air temperatures were recorded from 19 April through 9 September of 2010 at the location of GPS station FUFU. We attached a HOBO temperature sensor and recorder to the tetrahedra of station FUFU. Air temperatures were measured approximately one meter above the glacier's surface in five minute intervals.

2.3 Data Analysis

2.3.1 GPS Data

The GPS data were processed using the online Canadian Spatial Reference System-Precise Point Positioning (CSRS-PPP) analysis for Global Navigation Satellite System (GNSS) data post-processing (National Resources Canada, 2016). This analysis uses the precise GPS satellite orbit ephemerides to yield corrected coordinates with a constant accuracy, independent of station position or distance from network stations. Position timeseries were extracted from the output files for each time step and imported into MATLAB for analysis. We used the northing and easting GPS timeseries data to calculate the angle (α) Eq. (2.1) required to transform the position timeseries to the the along-flow, x_f, and transverse-flow, x_t, directions Eq. (2.2) and Eq. (2.3).

$$\alpha = \arctan\frac{y}{x} \tag{2.1}$$

Where x and y are easting and northing relative to their starting positions.

$$x_f = x\cos\alpha + y\sin\alpha \tag{2.2}$$

$$x_t = -x\sin\alpha + y\cos\alpha \tag{2.3}$$

The along-flow positions are smoothed using a locally weighted linear regression. For each data point to be smoothed we must first compute regression weights for each data point in the set span of 1440 data points, equivalent to six hours of data. The regression weights, w_i, associated with each data point, x_i, are calculated using a tricube function that gives the largest weight to the data point to be smoothed and zero weight outside of the span Eq. (2.4).

$$w_i = \left(1 - \left|\frac{x - x_i}{d(x)}\right|^3\right)^3 \tag{2.4}$$

Where w_i is the regression weight calculated for each of the 1440 data points x_i in the span of x and $d(x)$ is the distance along-flow between x and the farthest data point in the span x_i.

These values are used in calculating the weighted linear least-squares regression utilizing a first-degree polynomial. The 1440 regression weights are recalculated and the regression is preformed for each of the along-flow positions.

Horizontal Velocity Timeseries

We use these smoothed position timeseries to calculate velocities Eq. (2.5) by taking the first derivative of the along-flow position with respect to time (a time step of 15 seconds). It is necessary to filter and smooth velocity timeseries due to the noise in GPS measurements and the amplification of this noise by calculating velocities. We down-sampled the velocity timeseries (keeping every eighth data point, yielding a new sampling rate of two minutes) to reduce noise. We then applied a robust local regression Eq. (2.6), that is not influenced by a small fraction of outliers, to smooth the timeseries. A robust local regression was used based on its ability to recognize outliers. This method calculates the residuals from the locally weighted linear regression smoothing procedure described above then goes one step further and computes the robust weights for each data point in the prescribed span of 1440 points using the bisquare function Eq. (2.6). The outliers in the regression are assigned a lower weight, where a zero weight assigned to data outside the sixth absolute deviation from the median (6MAD).

$$\upsilon = \frac{d}{dt} x_f \tag{2.5}$$

$$w_i = \begin{cases} (1 - (\frac{r_i}{6MAD})^2)^2, & \|r_i\| < 6MAD \\ 0, & \|r_i\| \geq 6MAD \end{cases} \tag{2.6}$$

Where r_i is the residual of the i^{th} data point produced by the regression smoothing procedure, and MAD is the median absolute deviation of the residuals.

This velocity timeseries is smoothed again using both the local regression and robust weights; this is repeated for a total of five iterations. This method is similar to that of Podrasky and others

(2012) where a spline interpolation method was used to smooth the GPS position timeseries from multiple stations located on Jakobshavn Isbræ, Greenland.

We preformed an empirical error analysis of the GPS data and use simple error propagation to calculate errors in surface ice velocities. While this method is not robust it produces a more realistic error estimate by accounting for temporally correlated noise (i.e. colored or pink noise) (Moschas et al., 2013). We selected eleven days with little activity (stable temperatures, rainfall and ice velocities) and extracted 24 hours of along-flow positions from all active stations, a total of 25 samples, to calculate GPS position errors. The 24-hour along-flow position for each station was plotted with respect to time and was then fit with a linear line. The line of best fit was then subtracted from the along-flow positions.

$$S = \sqrt{\frac{1}{N-1}\sum_{i=1}^{N}|A_i - \mu|^2} \tag{2.7}$$

Where A is a vector of along-flow positions, S is the standard deviation of A, N is the number of observations, and μ is the mean of A.

We then calculated the standard deviation Eq. (2.7) of the residuals for each sample. Taking the mean of the 25 standard deviations calculated, we find a position error of ± 0.012 m in the along-flow direction. Using simple error propagation Eq. (2.8) we found that daily surface ice velocities can be resolved to ± 0.016 m d^{-1} and hourly velocities can be resolved to ± 0.39 m d^{-1}.

$$\delta v = \frac{\sqrt{2}\,\delta x}{dt} \tag{2.8}$$

Where δv is the error associated with velocity, δx is the error associated with position and dt is the timescale.

Vertical Component Timeseries

To account for the GPS stations that are advected downglacier by ice flow, we need to remove the associated change in surface elevation along the station's flow path to accurately measure local uplift. To determine the change in height of the glacier surface with time we remove the natural slope of the glacier. A linear fit was removed from the smoothed vertical data with respect to the distance along-flow (i.e. distance downglacier). This method was validated by comparing our results to a digital elevation model (DEM) from 2012 with a five meter resolution. Using a similar method as with the position data we calculate an error associated with the vertical component of station CNTR of ± 0.034 m. The vertical motion timeseries is used to determine temporary uplift that may be associated with water being stored at the glacier's bed during speed-up events.

2.3.2 Water Input Model

We use a water input model to extrapolate point measurements of air temperature and rainfall to glacier wide values. Due to the lack of mass balance measurements on Yahtse Glacier we use a simple degree-day model to estimate the total volume of melt and rain water input on daily timescales. The degree-day model is based on an empirical relationship between melt and air temperature, which is attributed to the high correlation of temperature with several dominating components of the energy balance equation (Ambach, 1988; Sato et al., 1984; Braithwaite and Olesen, 1990; Lang and Braun, 1990). Longwave atmospheric radiation and the sensible heat flux account for three fourths of the entire energy source for melt and are strongly affected by air temperature (Ohmura, 2001; Hock, 2003). The classical degree day model Eq. (2.9) relates melt, M (mm), during a period of n time intervals, Δt (d), to the sum of days with positive air temperatures, T^+ (°C), during the same period (Braithwaite, 1995; Hock, 2003).

$$\sum_{i=1}^{n} M = DDF \sum_{i=1}^{n} T^{+} \Delta t \tag{2.9}$$

The degree-day model uses a factor of proportionality named the degree day factor, DDF (mm d^{-1} $°C^{-1}$), that accounts for all terms of the energy budget. The low albedo of ice causes it to melt at a higher rate than snow, yielding different degree-day factors for a snow-covered surface and exposed ice. We use a mid-range value of 6 mm d^{-1} $°C^{-1}$, between ice and snow (Hock, 2003), because we do not have ablation rate measurements and our main cluster of GPS stations is in the upper ablation area.

Spatial variability in melt rates, related to decreasing melt with increasing elevation, is accounted for by dividing Yahtse into elevation bands and extrapolating air temperatures. Glacier hypsometry was found using 2012 GeoSAR digital elevation model (DEM) with a five meter resolution and a vertical uncertainty of ±1 m. The 2012 GeoSAR DEM was produced using a GeoSAR Interferometric Synthetic Aperture Radar and validated using LiDAR profiler data. A digital thermometer with a ten minute sampling rate was attached to the temporary GPS station FUFU from 29 May–9 September 2010 to record on-ice air temperatures (Section 2.2.2). The elevation-dependent air temperature is calculated using a locally derived summer lapse rate, β, Eq. (2.10) which is the ratio between the mean temperature difference, dT, and elevation difference, dz, between station FUFU and the weather station located near the terminus.

$$\beta = -\frac{dT}{dz} = 0.0051 \pm 0.0013 \frac{^{o}C}{m} \tag{2.10}$$

The daily volume of meltwater input, V_{melt}, was calculated using elevation-dependent air temperatures $T(z)$, in conjunction with the mid-range DDF of 6 mm d^{-1} $°C^{-1}$, and the area altitude

distribution $\rho(z)$, the total area in each elevation band Eq. (2.11). To find the glacier-wide volume of meltwater input I_{melt}, V_{melt} is integrated over the entire range of elevations Eq. (2.12).

$$V_{melt}(z) = T(z) \cdot DDF \cdot \rho(z), \quad for\ T > 0^oC \tag{2.11}$$

$$I_{melt} = \int V_{melt}\, dz \tag{2.12}$$

Where V_{melt} is volume of meltwater (m^3) for the elevation band z (m). Extrapolated air temperature $T(z)$ (°C) is found $T(z) = T^+\beta$, $\rho(z)$ is the area altitude distribution and I_{melt} the water input to the glacier from melt in cubic meters per day.

Rainwater input for the entire glacier I_{rain} is found by first calculating the volume of rainwater input for each elevation band Eq. (2.13) and applying the elevation-dependent air temperature to account for the rain/snow transition, then integrating over the range of elevations Eq. (2.14).

$$V_{rain}(z) = \rho(z)\, h_{rain}, \quad for\ T > 0^oC \tag{2.13}$$

$$I_{rain} = \int V_{rain}\, dz \tag{2.14}$$

where V_{rain} is the volume of rain water input for each elevation band, h_{rain} the precipitation measured at the terminus weather station.

The water input model produced realistic results when compared to daily air temperature and precipitation measured at the weather station. The water input model calculates daily meltwater input with an uncertainty of $\sigma = \pm\, 6.8 \cdot 10^5$ m^3 ($\pm$ 0.66 mm w.e.), daily rainwater input $\sigma = \pm\, 2.4 \cdot 10^4$ m^3 ($\pm$ 0.024 mm w.e.), and a total daily water input of $\sigma = \pm\, 7.0 \cdot 10^5$ m^3 ($\pm$ 6.9 mm w.e.). The main source of uncertainty in the melt model is the locally derived summer lapse rate used to calculate the elevation-dependent air temperature and the choice of a mid-range degree day factor (DDF). The summer lapse rate affects the model output uniformly throughout the season between years. Whereas the choice of a mid-range DDF will over estimate melt when the glacier is primarily snow covered early in the melt-season and underestimate melt when ice is exposed later in the melt-season.

A final caveat of the water input model is associated with the use of 24-hour averaged air temperatures and rainfall. The 24-hour averaged mean air temperature affects the quantity of rainfall calculated by the water input model. The rainfall may have occurred during the hottest time of day, thereby extending the rain/snow line further up-glacier. In this case the water input model would underestimate the amount of rainwater input. Using 24-hour averaged data does not allow us to compare subdaily rates of water input. While melt-water input is a more gradual process, a rainstorm can input the same volume of meltwater in a few hours. The assumptions used in calculating glacier-wide water input affect the magnitude of rain and meltwater input and

constrain the rates to daily averages. A specific volume of rainwater could be input within hours compared to the same volume of rainwater being input over the entire day. The model would equate these two water input events as having the same rate.

2.3.3 Glaciohydraulic Tremor

We use the glaciohydraulic tremor amplitude dataset produced by Bartholomaus and others (2015) as a proxy for subglacial discharge because of the difficulty of obtaining direct measurements on a tidewater glacier. We use this dataset to identify the timing of increased subglacial discharge near the terminus of Yahtse Glacier. Broadband seismometers were buried near the terminus of Yahtse Glacier, positioned to record activity on the lower 12 km of Yahtse from 2009 through 2011 (Larsen and West, 2009). The stations consisted of Guralp CMG-3Ts with Quanterra 330 digitizers and balers, each sensor having a flat response from 120 s to 50 Hz, and sampling rate between 100 and 200 samples per second. We use seismic data recorded by Bartholomaus and others (2015) at stations BOOM, 400 m from the western edge of the 2010 terminus; LUPN, installed on solid earth, east of the terminus; and STEW, west of the central cluster (strain diamond configuration) of GPS stations. Data from the vertical channel seismic recordings of ground velocity were analyzed by Bartholomaus and others (2015) in order to resolve tremor signals produced by subglacial discharge.

Bartholomaus and others (2015) statistically characterized seismic tremor by identifying the median power spectral density (PSD) within short-duration moving windows subsampled from a longer-duration waveform. Short-duration (20 s) waveforms with a 50% overlap were used to minimize the likelihood that a PSD samples a discrete event. The short-duration PSDs are then combined to determine the probability of the power at a given frequency reaching a specific level within the longer-duration time window previously set (McNamara and Buland, 2004). The mean power for 50% overlapping one day time windows was visually inspected for seasonal shifts in tremor amplitude. These conclusions do not differ when other time windows are used. Bartholomaus and others (2015) found glaciohydraulic tremor amplitude by taking the square root of the median PSD (with units of $(m/s)^2$ Hz^{-1}) over a range from 1.5 to 10 Hz, and integrating this quantity. The tremor amplitude is equal to the median, absolute ground velocity between 1.5 and 10 Hz as a consequence of Parseval's theorem (Press et al., 1988).

Using the tremor amplitude timeseries as a proxy for subglacial discharge as opposed to in situ observations requires careful interpretation of the results. Through simultaneous seismic, GPS and discharge measurements at Mendenhall Glacier, Bartholomaus and others (2015) found a relationship between subglacial discharge from Mendenhall Glacier and > 1 Hz tremor. Measurements of glaciohydraulic tremor at Yahtse Glacier show a distinct seasonal variation with higher tremor

amplitudes in the summer and lower tremor amplitude in the winter. A comparison of glaciohydraulic tremor with water input data reveal the coincidence of local maxima of water inputs and tremor amplitude. The proposed range of glaciohydraulic tremor (1.5–10 Hz) used by Bartholomaus and others (2015) is supported by seismic data recorded at Jakobshavn Isbræ, Greenland, and Columbia Glacier, Alaska. This empirical data demonstrates that glaciohydraulic tremor is a suitable proxy for subglacial discharge.

We use the peaks in glaciohydraulic tremor amplitude to identify the timing of peak subglacial discharge throughout the melt season and do not compare the magnitude of the local maxima of tremor with one another. Glaciohydraulic tremor amplitude is dependent upon water pressure which is in turn dependent upon the state of the subglacial drainage network. When the subglacial drainage network is inefficient a smaller quantity of water will create comparable signals to larger water inputs later in the melt-season. Therefore, late season subglacial discharge in an efficient drainage network may not be as well represented in the dataset (Gimbert et al., 2016).

2.3.4 Basal Hydrology Model

We investigate mechanisms causing the observed velocity variations on Yahtse Glacier by comparing our surface velocity measurements to basal velocities predicted by the coupled subglacial hydrology and sliding model developed by Bartholomaus and others (2011) and inverted by Brinkerhoff and others (2016). To simplify the relationship between the englacial and subglacial drainage systems the model treats both englacial and subglacial storage as an area-averaged quantity over the area of the glacier. This simplification reduces the model into a set of coupled ordinary differential equations which are solved for each time step.

The model glacier is a rectangular box with length L = 15 km, width W = 4 km, and depth H = 400 m, chosen to approximate the ablation area of Yahtse Glacier. The model assumes the bed is evenly distributed with uniform cavities formed on the downglacier side of bedrock bumps and that they respond to the evolution of water storage identically. The bedrock bumps are h meters tall by w_c meters wide, spaced λ_x and λ_y meters in the along-flow and transverse to flow directions, respectively.

The model assumes the glacier slides according to a power-law relationship (e.g. Bindschalder, 1983).

$$u_b = \frac{k\tau_b^n}{(P_0 - P)^\gamma} \tag{2.15}$$

where u_b is the basal velocity, k and γ are parameters, τ_b is the basal shear stress (e.g. Bindschadler, 1983; Jansson, 1995), P_0 is the ice overburden pressure and n is the flow law exponent.

The model also assumes the glacier is composed of a reservoir that encompasses both the englacial and subglacial drainage systems. They define an englacial reservoir with a static macroporosity, ϕ, that is well connected to the subglacial system with a varying capacity. Water pressure, $P(t)$, is used as a proxy for englacial water storage by assuming that storage in the englacial reservoir corresponds directly to subglacial water pressure.

$$\frac{dP}{dt} = \frac{\rho_w g}{LW\phi}\left(Q_{in}(t) - Q_{out}(t) - \frac{fLW}{h}\frac{dA_c}{dt}\right) \tag{2.16}$$

where ρ_w is the densities of water, g the acceleration due to gravity, $f = hw_c/\lambda_x\lambda_y$ is the dimensionless constant describing the cavity-forming capacity of the glacier's bed, and A_c the average cavity size (a proxy for subglacial storage).

This equation states that the change in water pressure is controlled by the flux into the system from the surface (Q_{in}) minus both the flux out the terminus (Q_{out}) and the change in the subglacial drainage system's capacity. The model uses the average cavity cross-sectional area, $A_c(t)$ as a parameter of the dynamic quantity of water stored subglacially. Cavity size is controlled by three dynamic processes that act to either open or close the cavity. Cavities grow as a result of both basal sliding over basal topography that causes the cavities to open on the downglacier side of bedrock bumps and turbulent heat generation which melts the cavity walls. Cavity growth is counteracted by the creep of ice (Nye, 1976).

$$\frac{dA_c}{dt} = u_b h + (1-\gamma_r)\left(\frac{\rho_w g}{\rho_i L_f}\right)\left(\frac{\lambda_x}{W}Q_{out}(t)\right)\nabla z_w - C_c A_c (P_0 - P)^n \tag{2.17}$$

where u_b is the sliding velocity, h is the height of the bedrock bumps, γ_r the Röthisberger's dimensionless constant (Röthlisberger, 1972), ρ_i is the density of ice, L_f the latent heat of fusion of ice, λ_x is the along-flow spacing of bedrock bumps, ∇z_w the hydraulic gradient of the cavity system, C_c the effective ice softness, P_0 the ice overburden pressure, and n is the flow law exponent.

The parameter ∇z_w is defined as the glacier surface slope divided by the cavity network sinuosity which we assume to be 3 (Kessler and Anderson, 2004). The model of Brinkerhoff and others (2016) constrained $A_c(t)$ to be positive to prevent the cavity from having a negative cross-sectional area and constrained $P(t)$ to lie between zero and P_0 to prevent the subglacial cavity from holding a vacuum (e.g. Schoof et al., 2012) and the englacial water table from overfilling the glacier.

The forcing function $Q_{in}(t)$ is specified by fitting a spline to our timeseries of daily water-input values calculated using the above mentioned water-input model. Bartholomaus and others (2011) used observations to specify Q_{out}. We do not have direct measurements of subglacial discharge on

Yahtse, instead we use the inverted model of Brinkerhoff and others (2016). The model of Brinkerhoff and others (2016) utilized the generalized Manning relationship to relate water pressure and channel size to the output flux $Q_{out}(t)$ (Walder, 1986).

$$Q_{out}(t) = rA_c^{\alpha}\left(\frac{P}{\ell}\right)^{\beta-1} \tag{2.18}$$

where r is the linear flux coefficient, α is the cavity flux exponent and β is the pressure flux exponent, ℓ is a gradient length scale which is used to approximate ∇z_w from P.

To solve for the subglacial water pressure, $P(t)$, and the average cavity cross-sectional area, A_c, (2.16) and (2.17) are integrated for each time step. The coupled ordinary differential equations are integrated using a 5th order backward difference formula (see `www.netlib.org/odepack`), performed using a real-valued variable-coefficient ordinary differential equation solver (Hairer et al., 1993). We use this system as a forward model to generate basal velocities and compare the predicted velocities to our observations of surface ice velocities. This model is also able to predict the output flux which we compare to our measurements of seismic tremor amplitude, our proxy for subglacial discharge.

We used the same constants and parameters determined by Bartholomaus and others (2011), presented in Table 2.2. The table includes the additional parameters used by including the generalized Manning relationship Eq. (2.18). We use the values determined by Brinkerhoff and others (2016) for the cavity flux exponent, pressure flux exponent, and cavity flux coefficient which are also shown in Table 2.2.

Param.	Value	Units	Description
ρ_w	1000	kg m^{-3}	Water density
ρ_i	900	kg m^{-3}	Ice density
g	9.8	m s^{-2}	Gravitational acceleration
L_f	$3.35{\cdot}10^5$	J kg^{-1}	Latent heat of fusion for ice
L	15	km	Glacier length
W	4	km	Glacier width
H	400	m	Glacier thickness
h	1	m	Bedrock bump height
w_c	5	m	Bedrock bump width
λ_x	10	m	Bedrock bump along-flow spacing
λ_y	10	m	Bedrock bump transverse to flow spacing
P_0	3.6	MPa	Ice overburden pressure
$k\tau_b^n$	$8 \cdot 10^{-4}$	m a^{-1} Pa$^{\gamma}$	Scaled driving stress
γ_r	0.303		Röthlisberger's dimensionless constant
γ	0.22		Pressure sliding exponent
k	$3 \cdot 10^{-4}$		Sliding law parameter
n	3		Glen's flow law exponent
f	0.05		Bedrock form factor
ϕ	0.007		Englacial reservoir static macroporosity
∇z_w	0.01		Hydraulic gradient of cavity system
C_c	$1.77{\cdot}10^{-25}$		Effective ice softness
α	5/4		Cavity flux exponent
β	3/2		Pressure flux exponent
r	-0.2	Pa$^{1-\beta}$ s^{-1} m$^{\beta+2(1-\alpha)}$	Cavity flux coefficient
ℓ	45	km	Gradient length scale

Table 2.2. Basal Hydrology Model Parameters. Symbolic constants and parameters used in the basal hydrology model, their value, units, and a description of the parameter.

Chapter 3

Results

The combination of weather, seismic and GPS measurements has produced a three year dataset beginning 11 June 2009 and ending 11 September 2011. The recording periods of the various GPS stations are shown in Table 2.1. This dataset captures the dynamic behavior of Yahtse Glacier on daily to seasonal timescales. The weather data was then used as input to a basal velocity model where the ice velocity timeseries is compared to modeled basal velocity. The glaciohydraulic tremor amplitude record is used as a proxy for subglacial discharge and is compared to the model's predictions of subglacial discharge.

Key features of the velocity timeseries are the continued presence of speed-up events and extra slowdowns. We define a speed-up event as a positive velocity variation where surface ice velocities increase by a minimum of 10% of the previous stable ice velocity over a maximum of 10 days. The 10% increase in velocity must be observed by the GPS station furthest down-glacier. We define an extra slowdown as a negative velocity variation where the surface ice velocity following a speed-up event stabilizes to a minimum of 10% below ice velocities before the speed-up event. A 24-hour mean velocity is used to determine stable ice velocity before and after the speed-up event.

Three years of simultaneously collected data from Yahtse Glacier are shown in Figure 3.1. Mean daily air temperature ($\sigma = \pm 1°C$) and daily rainfall ($\sigma = \pm 4\%$) measured at our weather station near the terminus of Yahtse are shown in Figure 3.1a. These data were used in the water input model (WIM) to calculate glacier-wide volume of water input ($\sigma = \pm 6.9$ mm w.e.). The cumulative volume of water input is calculated annually and shown in Figure 3.1b, along with the contributions of melt and rainwater input. The daily volume of meltwater, rainwater and total water input is shown in Figure 3.1c. The complete surface ice velocity record is presented in Figure 3.1d, where data from our permanent GPS stations CNTR and COED are in blue and red respectively. Daily surface ice velocities are resolved to ± 0.016 m d^{-1}. Glaciohydraulic tremor amplitude, our proxy for subglacial discharge, is shown in Figure 3.1e for three seismic stations distributed around the terminus of Yahtse Glacier.

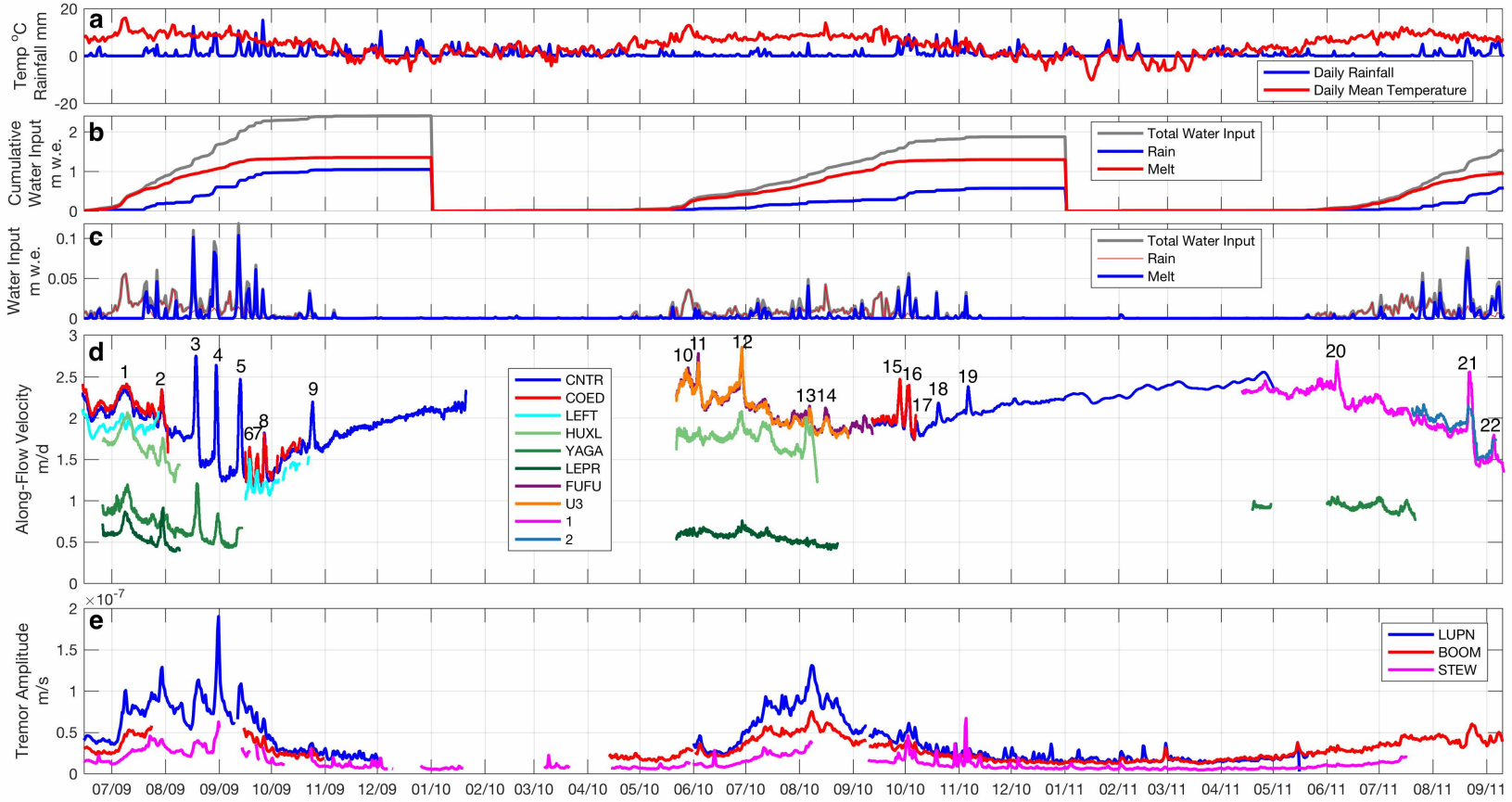

Figure 3.1. 2009–2011 Timeseries dataset. Timeseries data from 14 June 2009 through 11 Sept 2011. (a) Daily mean air temperature (°C) in red and daily rainfall (mm) in blue. Water input model (b) cumulative annual water input and (c) daily water input in meters water equivalent, with total water input (gray), meltwater input (red), and rainwater input (blue). (d) Along-flow surface ice velocity (meters per day) for each GPS station (indicated by color) are displayed. Speed-up events are indicated with their corresponding number printed above the local maxima. (e) Glaciohydraulic tremor amplitude in meters per second for seismic stations LUPN (blue), BOOM (red) and STEW (magenta).

3.1 Horizontal Ice Motion

3.1.1 Seasonal Flow Characteristics

The GPS velocity record revealed a recurring seasonal pattern of a summer slowdown followed by a winter speed-up. This general pattern is superimposed with short duration (on the order of days to weeks) speed-up events and extra slowdowns. The 2009 melt-season experienced a summer slowdown and a winter speed-up as well as nine speed-up events and two extra slowdowns. GPS stations were first deployed on Yahtse on 15 June 2009 where our main station CNTR (11 km) located in the ablation area recorded a speed of 2.2 m d^{-1}. Station CNTR recorded four speed-up events and two extra slowdowns before reaching the minimum velocity of 1.2 m d^{-1} on 1 September 2009, a 45% decrease from the beginning of the melt-season. Station YAGA (41 km) recorded initial velocities of 0.85 m d^{-1} on 25 June 2009 and a velocity of 0.45 m d^{-1}, 76 days later, on 9 September. Four more speed-up events were recorded before the onset of the winter speed-up on 1 October 2009. One additional speed-up event was experienced after the onset of the winter speed-up but no extra slowdown was coupled with this speed-up event. The pre-melt-season speed of 2.2 m d^{-1} was reached on 19 January 2010, 110 days after the onset of the winter speed-up.

The 2010 melt-season is characterized by a summer slowdown and winter speed-up superimposed with seven speed-up events and one extra slowdown. Our observations of the 2010 melt-season began on 21 May 2010 where our station in the ablation area FUFU (10 km) recorded an initial speed of 2.2 m d^{-1}. Four speed-up events and one extra slowdown was experienced before minimum speed of 1.8 m d^{-1} was reached following speed-up event 13 (SE13) on 9 August 2010. Yahtse experienced four more speed-up events before the onset of the winter speed-up on 10 October 2010. After the onset of the winter speed-up Yahtse experienced two more speed-up events, neither coupled with an extra slowdown. The pre-melt-season speed of 2.2 m d^{-1} was restored on 18 December 2010, 69 days after the onset of the winter speed-up.

The 2011 melt-season began with ice velocities of 2.3 m d^{-1} measured on 15 April by station ONE (11.2 km). The 2011 melt-season was marked by three speed-up events and two extra slowdowns. Ice velocities reached a minimum of 1.4 m d^{-1} on 9 September, a 39% decrease from the beginning of the melt-season following SE21. Our study ended on 11 September 2011 so we do not have any measurements of the 2011 winter speed-up. We did record a final velocity of 1.3 m d^{-1} on station ONE on 11 September 2011.

3.1.2 Speed-Up Events

Throughout the three melt-seasons Yahtse experienced a total of 21 speed-up events superimposed on seasonal velocity trends. These speed-up events were observed by GPS stations located

from 11–52 km up-glacier. The 2009 melt-season was marked by a total of nine speed-up events, the first beginning on 28 June and the last beginning on 21 October 2009. During the 2009 melt-season we observed the three largest speed-up events, SE3–5. SE3 began on 15 August and reached a peak velocity of 2.8 m d^{-1} after two days, a 55% increase. SE4 began seven days after the conclusion of SE3, on 27 August, and reached a peak velocity of 2.6 m d^{-1} after three days, a 77% increase. The third successive speed-up event, SE5, began eight days after the conclusion of SE4 on 9 September, and reached a peak velocity of 2.5 m d^{-1} after three days, an 84% increase. Station YAGA (42 km) located in the middle of the accumulation area was active until 9 September 2009 and recorded SE3 and SE4. YAGA recorded a peak velocity of 1.3 m d^{-1}, an 127% speed increase for SE3 and a peak velocity of 1.0 m d^{-1}, an 108% increase for SE4.

Nine speed-up events were recorded in the 2010 melt-season. SE10, the first speed-up event of 2010, began on 23 May 2010 and the last speed-up event of the season, SE19 began on 3 November 2010. A peak annual velocity of 2.9 m d^{-1}, a 19% increase from prior to the event, was reached during SE12 by station U3 (12 km). The largest magnitude speed-up event of 2010 (measured by our main GPS station CNTR) was SE16 which began on 29 September, where a peak velocity of 2.3 m d^{-1} was reached, a 25% increase.

We recorded a total of three speed-up events from 1 January–11 September 2011, the end of our study. The first speed-up event of 2011, SE20, began on 4 June 2011 with an initial velocity of 2.4 m d^{-1}, and reached a peak velocity of 2.7 m d^{-1} after one day, a 15% increase. SE21, the fourth largest magnitude speed-up event observed throughout the study, began on 19 August with an initial velocity of 1.9 m d^{-1} and reached a peak velocity of 2.6 m d^{-1} after two days, a 38% increase. The final speed-up event of our timeseries, SE 21, followed SE20 by eight days, had an initial velocity of 1.5 m d^{-1} and reached a peak velocity of 1.8 m d^{-1} after two days, a 20% increase.

3.1.3 Extra Slowdowns

A total of five extra slowdowns were observed throughout the three year study period. The first extra slowdown observed was coupled with SE3 in the 2009 melt-season. The ice velocity measured by station CNTR prior to SE3 was 1.8 m d^{-1} on 15 August. By 18 August the ice velocity peaked to 2.8 m d^{-1} then fell to 1.4 m d^{-1} on 20 August, a 19% slower velocity than before the speed-up event. Ice velocity slightly increased to 1.5 m d^{-1} by the onset of SE4 on 27 August. Following SE4, ice velocities fell to 1.3 m d^{-1}, a 15% decrease from before the event. Both extra slowdowns were also observed by station YAGA in the accumulation area 42 km from the terminus. YAGA recorded a 10% slowdown following SE3 and a 3% slowdown following SE4.

One extra slowdown was recorded during the 2010 melt-season. SE11, the second speed-up event of 2010, began on 1 June with an initial velocity of 2.4 m d^{-1} recorded at station FUFU (10 km). After reaching a peak velocity of 2.8 m d^{-1} one day later, a 17% increase, the ice velocity fell to 2.1 m d^{-1} three days later on 5 June 2010, an 11% decrease.

Two extra slowdowns were observed during the 2011 melt-season. The first extra slowdown of 2011 was coupled with the first speed-up event of the season, SE20. SE20 began on 4 June 2011 with an initial velocity of 2.4 m d^{-1} at station ONE (11.2 km). Ice velocities peaked to 2.7 m d^{-1} the next day, a 15% increase. Ice velocities then fell over the next five days, falling to 2.1 m d^{-1}, a 10% decrease, by 10 June. The next speed-up event, SE21, began on 19 August, 79 days later. SE21 began with an initial velocity of 1.9 m d^{-1} and peaked to 2.6 m d^{-1} after two days, a 38% increase. Ice velocities then fell for another two days until reaching 1.4 m d^{-1}, a 23% decrease, by 25 August 2011.

3.2 Vertical Ice Motion

A comparison between the water input, surface ice velocity, and detrended surface height timeseries are shown in Figure 3.2. The surface ice velocity timeseries from station CNTR is shown in Figure 3.2b. The vertical component of the GPS data recored at station CNTR during the 2009 melt-season is detrended to see changes in surface elevation over time. The vertical component of the GPS position data was detrended with respect to distance traveled downglacier using a linear line of best fit. This linear line of best fit was removed from the raw position data and plotted against time (Figure 3.2c).

Station CNTR was drilled into the ice and therefore recorded the motion of a point just below the ice surface, independent of ablation. We determined an error of $\pm$3.4 cm associated with the vertical component of the GPS position timeseries (Section 2.3.1). Changes in vertical displacement can also be attributed to vertical strain, motion parallel to the bed slope, dilation of subglacial sediments and bed separation (Howat et al., 2008).

Periods of rapid surface uplift were temporally coincident with the three largest horizontal speed-up events (SE 3–5) and periods of intense rainfall in 2009 (Figure 3.2). Surface uplift associated with SE3 was recorded by our main GPS station CNTR that recorded a total of 9 cm of uplift at a rate of 3 cm d^{-1}. Following the uplift the ice surface fell 22 cm at a rate of 2 cm d^{-1}. During SE5 Yahtse experienced 2 cm of uplift at a rate of 1 cm d^{-1}. Once reaching the maximum uplift the ice surface began to subside at a rate of 2 cm d^{-1} lowering a total of 15 cm. CNTR recorded a total uplift of 7 cm associated with SE5 at a rate of 2 cm d^{-1}, this was followed by surface lowering of 11 cm at a rate of 1 cm d^{-1}. While we expect surface uplift to be a common phenomena associated with large water input events and cavity formation we were unable to record clear indications of

surface uplift for the remainder of our study period due to the lack of one consistent GPS station recording throughout the entire melt-season in 2010 and 2011.

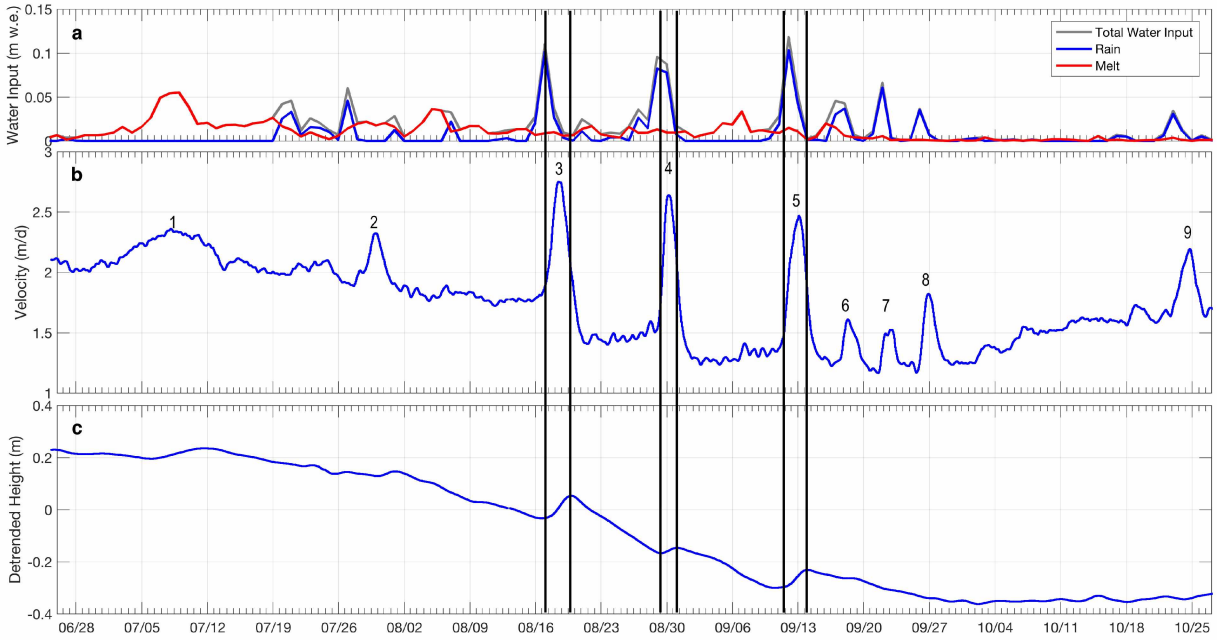

Figure 3.2. 2009 Vertical Motion. The 2009 melt-season comparison between (a) water input time-series (m w.e.), (b) Surface ice velocity (m d^{-1}) from station CNTR is plotted with respect to time where numbers refer to the speed-up event name. (c) The vertical component of the GPS data from station CNTR detrended with respect to distance downglacier using a linear fit produces a detrended surface height record that is plotted here with respect to time. Gray vertical lines mark the beginning and end of change in vertical height on the CNTR GPS record.

3.3 Glaciohydraulic Tremor

We observe an increase in tremor amplitude from the mean amplitude of $4.0 \cdot 10^{-8}$ m s^{-1} to the melt-season mean amplitude of $7.9 \cdot 10^{-8}$ m s^{-1} from 3 July thorough 3 October 2009. On 3 October tremor amplitudes dropped to a sustained level of $2.4 \cdot 10^{-8}$ m s^{-1}. The initial increase in tremor amplitude followed a period of high meltwater generation, lagging the beginning of SE1 by five days. Tremor amplitude peaked closely following the first eight speed-up events, following maximum water input by an average of two days, and following the peak velocity during the speed-up events by one day. There is not a pronounced peak in amplitude that corresponds with SE9, the last speed-up event of the 2009 melt-season.

Tremor amplitudes rose above the pre-melt-season level of $2.9 \cdot 10^{-8}$ m d^{-1} on 20 June 2010 with a seasonal mean amplitude of $6.8 \cdot 10^{-8}$ m s^{-1}. Tremor amplitude dropped below the melt-season level on 24 September 2010 and maintained a mean amplitude of $2.6 \cdot 10^{-8}$ m s^{-1} throughout the winter. Prior to the increased melt-season amplitude, tremor amplitude briefly peaked on 3 June 2010, following SE11 by two days. Seismic station LUPN stopped recording on 19 May 2011,

leaving station BOOM to record throughout the 2011 melt-season. Tremor amplitude on station BOOM started increasing above the winter average on 10 May 2011 but produced only one distinct peak that coincided with SE21, lagging behind peak water input by 2.5 days and behind peak ice velocity by 1.5 days.

The 2009 melt-season produced elevated tremor amplitudes for 92 days, four days shorter than the 96 day long 2010 melt-season. We observe local maxima later in the 2010 melt-season that are tied with SE14–16, after tremor amplitudes drop to the pre-melt-season level. Peak tremor amplitude followed peak rainfall by one day for SE14, matched peak rainfall for SE15 and preceded peak rainfall by 0.5 days for SE16. Tremor amplitude recorded by station STEW was higher than usual at the end of the 2010 melt-season with peaks corresponding with the two late season speed-up events.

3.4 Basal Hydrology Model

We applied the basal hydrology model developed by Bartholomaus and others (2011) and adapted by Brinkerhoff and others (2016) to Yahtse Glacier and compare the results to our velocity and tremor amplitude measurements. This model was developed to describe the basal hydrology of Kennicott Glacier, a 43 km long alpine, land-terminating glacier located in the Wrangell Mountains of southcentral Alaska. Bartholomaus and others (2011) applied the model to the lower 15 km of Kennicott Glacier to represent the ablation area, we similarly apply the model to the lower 15 km of Yahtse Glacier. We specify the forcing function $Q_{in}(t)$ using the output of the water input model, a similar degree-day model used by Bartholomaus and others (2011) in application to Kennicott. Our $Q_{in}(t)$ spans three consecutive melt-seasons beginning 11 June 2009, ending 11 September 2011.

The basal hydrology model results along with the forcing function and observations for comparison are shown in Figure 3.3. We used the daily total water input (Figure 3.3a) from 29 June 2009 through 10 September 2011 calculated by the water input model to specify the input flux, the forcing function $Q_{in}(t)$ of this model. To compare our observations of surface ice velocity with the modeled basal velocity we added a constant value of 1.3 m d^{-1} to $u_b(t)$ to account for ice deformation. This value is the 2009 minimum surface ice velocity which we assume to have occurred at zero basal motion. The observed surface ice velocity timeseries is composed of observations from GPS stations CNTR, FUFU, and ONE (Figure 2.1) to cover the entire time period. The comparison between modeled and observed surface ice velocity is shown in Figure 3.3b. The evolution of englacial and subglacial water storage is shown in Figure 3.3c, using our proxy for englacial water storage, water pressure (P), and proxy for subglacial water storage, average conduit cross-sectional area (A_c). Figure 3.3d shows modeled subglacial discharge or output flux, Q_{out}modeled,

compared with our proxy glaciohydraulic tremor amplitude, Q_{out}proxy. To compare tremor amplitude covering the entire time period we use tremor amplitude recorded on seismic station LUPN (Figure 2.1) from 29 June 2009–31 March 2010 and seismic station BOOM from 1 April 2011–10 September 2011.

The results of the basal hydrology model show the relationship between water input and the corresponding variations in velocity and subglacial discharge. While the model was not able to reproduce long timescale variability in velocity, it was able to reproduce shorter duration velocity variations (speed-up events). The modeled velocity variations parallel the magnitude of water input rather than the magnitude of observed speed-up events. The seven largest velocity variations produced by the model correspond to SE1, SE3–5, SE10, SE16, and SE21.

The model was able to reproduce both the duration and peak timing of the speed-up events. All durations are replicated to within a day except for SE1 which lasted fourteen days but was modeled as lasting seven days. SE3–5 and SE21 were modeled with peak velocities proceeding observed peak velocities by 1.0, 0.2, and 0.4 days respectively. The peak velocity produced by the model for these three speed-up events lagged behind peak water input by 0.5, 0.9, and 0.7 days respectively. The modeled peak velocity for SE21 occurred 0.5 days before the observed peak velocity, 0.7 days after peak water input. Peak modeled ice velocity for SE1 occurred 0.7 days after the observed peak ice velocity. The peak modeled ice velocity for SE10 and SE16 occurred after observed peak velocity by 1.3 days and 0.7 days respectively.

The modeled results for englacial and subglacial water storage covary with the forcing function throughout the timeseries. The model produces large short-lived variations of englacial storage (Figure 3.3c) while the coincident peaks in subglacial storage do not dissipate as quickly and are less pronounced. The average conduit cross-sectional area, A_c, does not ever reach zero, with a minimum value in the winter of 2.5 m^2, or an average conduit radius of 0.9 m. A_c reached peak values during the seven speed-up events reproduced by the model, reaching a maximum cross-sectional area of 69.2 m^2 during SE6, a radius of 4.7 m, after SE6. A_c reached an average area of 55.9 m^2, or average radius of 4.2 m, across the seven speed-up events.

Similar to the melt-season tremor amplitude increase, pressure, P, remains above zero throughout each melt-season while returning to zero in the winter. The late melt-season drop in amplitude corresponds temporally with the onset of winter speed-up during 2009 and 2010. The winter speed-up of 2009 begins on 1 October while P is decreasing (a value 50% lower than the preceding local minima) by 3 October 2009. Similarly the 2010 winter speed-up begins on 10 October and P is decreasing by 14 October 2010.

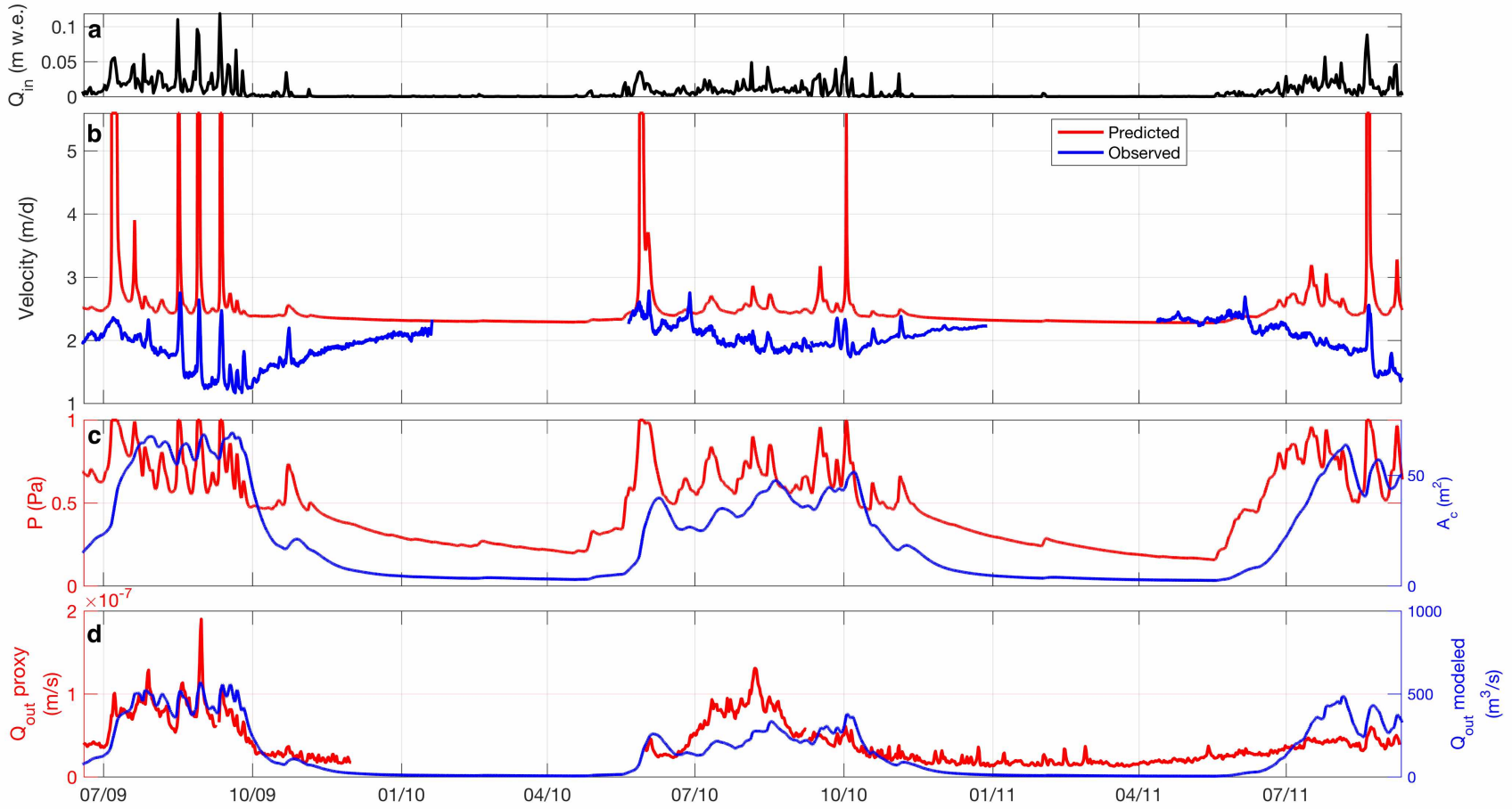

Figure 3.3. Basal Hydrology Model Results. (a) Q_{in} (m w.e.) is the daily total water input determined by the water input model. (b) Predicted surface velocity (m d^{-1}) and observed surface ice velocity are plotted in red and blue respectively for comparison. (c) Modeled water pressure, P (Pa), our proxy for englacial water storage and average conduit cross-sectional area, A_c (m^2), our proxy for subglacial water storage are plotted in red and blue respectively. (d) This model calculates the flux out the terminus, $Q_{out}modeled$ (m^3 s^{-1}), for subglacial discharge is plotted in blue. Our proxy for subglacial discharge, $Q_{out}proxy$ (m s^{-1}), tremor amplitude is plotted in red for comparison.

The model was able to reproduce both the seasonal increase in subglacial discharge and shorter period peaks observed in our glaciohydraulic tremor amplitude record (Figure 3.3d). The 2009 and 2011 melt-seasons had the strongest correlation between modeled and proxy water flow out, Q_{out}, with closely covarying amplitudes during the beginning and end of the melt-season. The model shows the existence of the seasonal increase in Q_{out} for the 2010 melt-season but does not reproduce the magnitude or timing as well as it did for the 2009 melt-season. During each melt-season the model produced peaks that correspond with peaks in the tremor amplitude record. The model produces peaks in Q_{out} an average of 1.5 days before the observed peaks in tremor amplitude for the speed-up events coupled with extra slowdowns (SE3, SE4, and SE21). The model produces peaks in Q_{out} an overage of 0.3 days after the observed peaks in tremor amplitude for the rest of the reproduced speed-up events.

The basal hydrology model was able to reproduce 19 out of 22 speed-up events from 2009–2011. The model was not able to reproduce the magnitudes of the speed-up events and modeled an additional eight speed-up events that were not observed by our GPS stations. The model was not able to reproduce the extra slowdown events the seasonal trend of a summer slowdown and winter speed-up. The use of the Manning relationship to calculate Q_{out} was successful in reproducing the elevated discharge throughout the summer. The model showed increased subglacial discharge following the speed-up events.

Chapter 4
Discussion

Three years of observations of Yahtse Glacier has revealed the control late-summer rainfall has on average annual ice velocities. It has been argued that wintertime flow speeds are inversely related to the quantity of melt from the preceding summer (Burgess et al., 2013a). Our high resolution monitoring of ice velocities and water inputs over three melt-seasons has shown that the presence of heavy rainfall over several days will amplify the summer slowdown. The minimum ice velocity reached during the melt-season impacts flow speeds until mid-winter. Measurements of glaciohydraulic tremor, which we use as a proxy for subglacial discharge, indicate the changing volume of water in subglacial storage and the dynamic response of the isolated cavity system is the source of the seasonal trends in ice velocity.

4.1 Glacier Flow on Seasonal Timescales

Surface ice velocities from 2009–2011 are compared in Figure 4.1, emphasizing the repeated pattern of a summer slowdown and winter speed-up. Ice velocities measured in our main cluster of GPS stations are plotted with respect to the day of year. Each melt-season follows a similar trend of decreased ice speeds superimposed with speed-up events from June to mid-August (Figure 4.1). This decrease in flow velocity is irregular and stepwise, where the glacier speeds up before slowing down. Schoof (2010) showed that summer slowdowns are the result of a seasonal switch from an unchannelized to channelized drainage system. The stepwise slowdown observed indicates that the discrete pulses of increased water input that precede each speed-up event cause the subglacial drainage system to increase its efficiency, resulting in decreased basal motion after the water is accommodated.

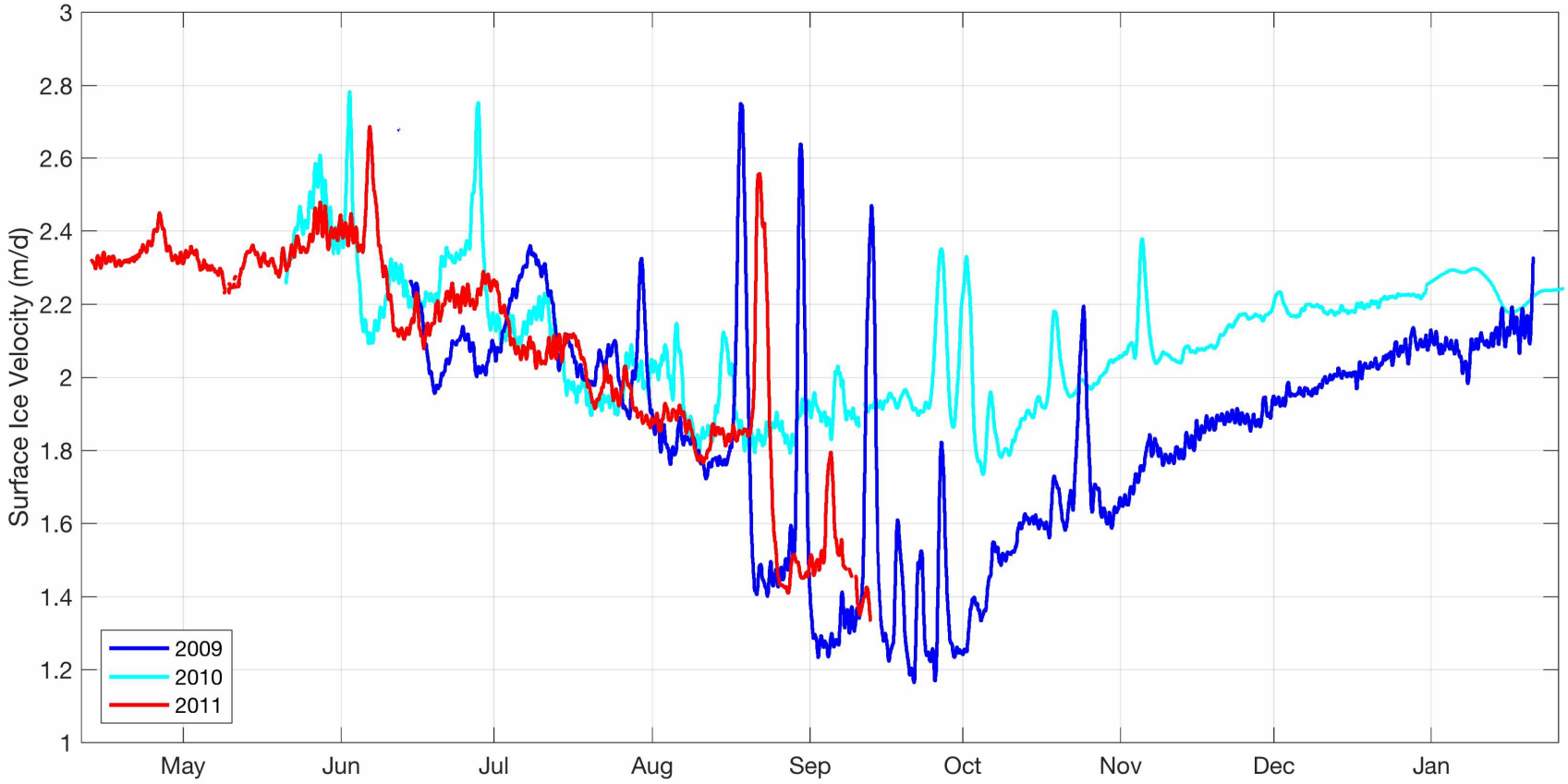

Figure 4.1. Comparison of Annual Ice Velocities. Surface along-flow ice velocity throughout study period plotted with respect to day of year. The ice velocity record from 2009 is plotted in blue and was recorded by station CNTR (11 km). Ice velocities from 2010 are plotted in cyan using data from station FUFU (10 km) from May–August 2010 and station CNTR from September through January 2011. The ice velocity recorded at station ONE (11 km) from April–11 September 2011 is plotted in red.

4.1.1 Summer Slowdown

The early melt-season, from May through August, is characterized by an overall slowdown modulated by speed-up events and extra slowdowns. This slowdown indicates the evolution of the subglacial drainage system towards a more channelized and connected configuration.

The beginning of the melt-season exhibits the highest stable ice flow speeds of the year which indicates the inefficiency of the subglacial drainage system. Hodge (1974) argued that sliding speed is controlled by the amount of basal water stored in subglacial cavities, where maximum storage occurs early in the melt-season before an efficient basal drainage system can be developed. The stable high flow rates are disrupted when water inputs first reach the bed at the beginning of the melt-season (e.g. SE1, SE10, and SE20 (Figure 3.1)) causing water pressures to increase, cavities to enlarge, and basal sliding to increase (Fountain and Walder, 1998). Ice velocity will decrease when water inputs produce a great enough englacial flux (and resulting pressure perturbation) that will enlarge cavity orifices unstably and spawn an R channel system (Kamb, 1987).

Speed-up events have been observed on numerous glaciers (Willis, 1995) and have been used to infer basal motion in the context of changing basal conditions and the evolution of the subglacial drainage system (e.g. Kamb et al., 1994). Speed-up events followed by extra slowdowns have been observed on Columbia Glacier (Meier et al., 1994; Kamb et al., 1994), Unteraargletscher (Gudmundsson et al., 2000), and on Hansbreen (Vieli et al., 2004). These observations indicate the speed-up events have a lasting effect on the structure of the subglacial drainage system. Speed-up events are produced when the water input to the glacier's bed exceeds the ability of the subglacial drainage system to transport the water. This water is accommodated as subglacial conduits grow by frictional melting of the walls or the rate of water input drops (Bartholomaus et al., 2011). As the subglacial drainage system becomes channelized water will move from the high-pressure linked cavity system towards the lower-pressure conduits (Munson et al., 2005). This movement of water from the areally extensive linked-cavity system to the newly expanded conduits increases contact between the glacier and its bed, reducing basal motion (Iken and Bindschadler 1986; Bindschadler 1983).

Vieli and others (2004) observed speed-up events on Hansbreen, a 16-km long tidewater glacier in Spitabergen, Svalbard. These speed-up events were only observed in the ablation area, indicating that a significant change in the drainage system only took place on the lower 10 km of the glacier (Vieli et al., 2004). Speed-up events are observed on all GPS stations on Yahtse, extending 52 km from the terminus to station LEPR. Not only did the GPS stations located in the accumulation area observe speed-up events but they also recorded the coupled slowdowns (Figure 3.1). This indicates that the subglacial drainage system experiences changes in both the ablation and accumulation areas throughout the melt-season.

The downward velocity trend of the summer slowdown deviates in mid-August (Figure 4.1) when heavy rainfall triggered large speed-up events coupled with extra slowdowns in 2009 and 2011 (Figure 3.1). In 2009 two periods of heavy rainfall triggered (Section 4.2) two speed-up events coupled with extra slowdowns, SE3 on 15 August and SE4 on 27 August 2009, resulted in ice velocities dropping 0.5 m d^{-1} from before SE3. Yahtse experiences four additional speed-up events but no other extra slowdowns before the onset of the winter speed-up. In 2011 four days of heavy rainfall triggered SE21 on 19 August 2011 that was coupled with an extra slowdown dropping velocities by 0.4 m d^{-1}. In August 2010 there were no large storms to trigger similar extra slowdowns, resulting in Yahtse maintaining this higher early August speed until the onset of the winter speed-up in early October.

The periods of heavy rainfall triggered the large magnitude speed-up events coupled with the extra slowdowns that amplified the summer slowdown in 2009 and 2011 (Section 4.2). Observations of simultaneous uplift during these speed-up events as well as the relative timing of peak ice velocity indicates the extra slowdowns are a consequence of the isolated cavity system, this will be discussed further in Section 4.3.

4.1.2 Winter Speed-Up

While the summer slowdown is caused by the release of water in storage and the channelization of the subglacial drainage system, the winter speed-up is caused by the remaining water stored in isolated cavities. Isolated and interconnected subglacial cavities can coexist (Weertman, 1964). During the late melt-season, the drainage system is efficient and the enlarged subglacial channels require a large water flux to sustain them (Fountain and Walder, 1998). As water input decreases late in the season the inward creep of ice will remain unchecked and will close the conduits. When the R channels collapse additional water input can no longer drain freely, causing both subglacial water pressure and storage to rise (Iken and Truffer, 1997). At this point the isolated cavities will produce a lubricating effect as subglacial water pressures decrease and the interconnected cavities shrink at the end of the melt-season (Iken and Truffer, 1997). These isolated cavities collect basal and internal meltwater, increasing in size and pressure throughout the winter, leading to increased basal motion (Iken and Truffer, 1997).

The winter speed-up begins in early October and persists until January when pre-melt-season speeds are reached. The winter speed-up of 2009 began with an initial speed of 1.2 m d^{-1} on 1 October and lasted 110 days, ending on 19 January 2010 when the pre-melt-season speed of 2.2 m d^{-1} was reached. One speed-up event, SE9, occurred during the 2009 winter speed-up. The presence of SE9 did not affect the winter speed-up. The winter speed-up of 2010 began with an initial speed of 1.8 m d^{-1} on 10 October 2010 and lasted 69 days, ending when the pre-melt-season

speed of 2.2 m d^{-1} was reached on 18 December 2010. During the winter speed-up of 2010, two speed-up events occurred, SE18 and SE19. Neither event affected flow speeds after its conclusion.

The minimum summer speed, reached on 1 September 2009 and 10 August 2010, controls ice velocities until early-winter when pre-melt-season speeds are restored. The extra slowdown associated with SE4 produced a minimum speed of 1.2 m d^{-1} in 2009, whereas the minimum speed reached in 2010 was 1.8 m d^{-1} following SE13. As a result the 2009 average annual velocity was 1.8 m d^{-1} compared to the 2010 average annual velocity of 2.1 m d^{-1}, a 15% difference between years.

4.1.3 Controls on Glacier Flow

Burgess and others (2013a) found an inverse relationship between wintertime glacier velocity and the volume of melt from the preceding summer, a relationship we do not observe on Yahtse Glacier. This relationship was identified using wintertime ice velocities for 160 Alaskan glaciers and compared to total summertime melt-water input (Burgess et al., 2013b). The slowdowns that occurred over the summers of 2009 and 2011 were similar to each other in magnitude and timing. The slowdown over the summer of 2010 was different by not reaching the lower summer minimum speeds reached in both 2009 and 2011. In order to determine if there is a correlation between the lower winter velocity and meltwater input we compare meltwater and rainwater input between 2009–2011. A comparison of cumulative annual water input from 2009–2011 is shown in Figure 4.2. The cumulative annual meltwater input in meters water equivalent for 2009–2011 is shown in Figure 4.2a from May through December of each year. The cumulative annual rainwater input, calculated by our water input model, is shown in Figure 4.2b with units of meters water equivalent.

Our velocity data shows a correlation between lower summer speeds and lower winter and annual speeds. We see an additional correlation between higher cumulative annual rainwater input and lower ice velocities. Cumulative meltwater input is compared in Figure 4.2a, while the first melt event of 2010 preceeds that of 2009 and 2011 by approximately a month the overall seasonal trend is similar. Only 0.08 m w.e. more meltwater was input in 2009 than in 2010, a 6% difference. The biggest difference between 2009 and 2010 is seen in Figure 4.2b when comparing the cumulative rainwater input. The annual cumulative rainwater input in 2009 exceeds 2010 by 0.48 m w.e., a 59% difference.

A correlation exists between lower wintertime ice velocity and higher rainwater input. Our high resolution monitoring of Yahtse Glacier reveals that ice velocity deviates in mid-August when short periods of heavy rainfall trigger extra slowdowns. The summer minimum speed impacts

wintertime flow velocities until mid-winter. Therefore a lower summer minimum speed results in lower speeds throughout the winter which reduce the annual flow velocity.

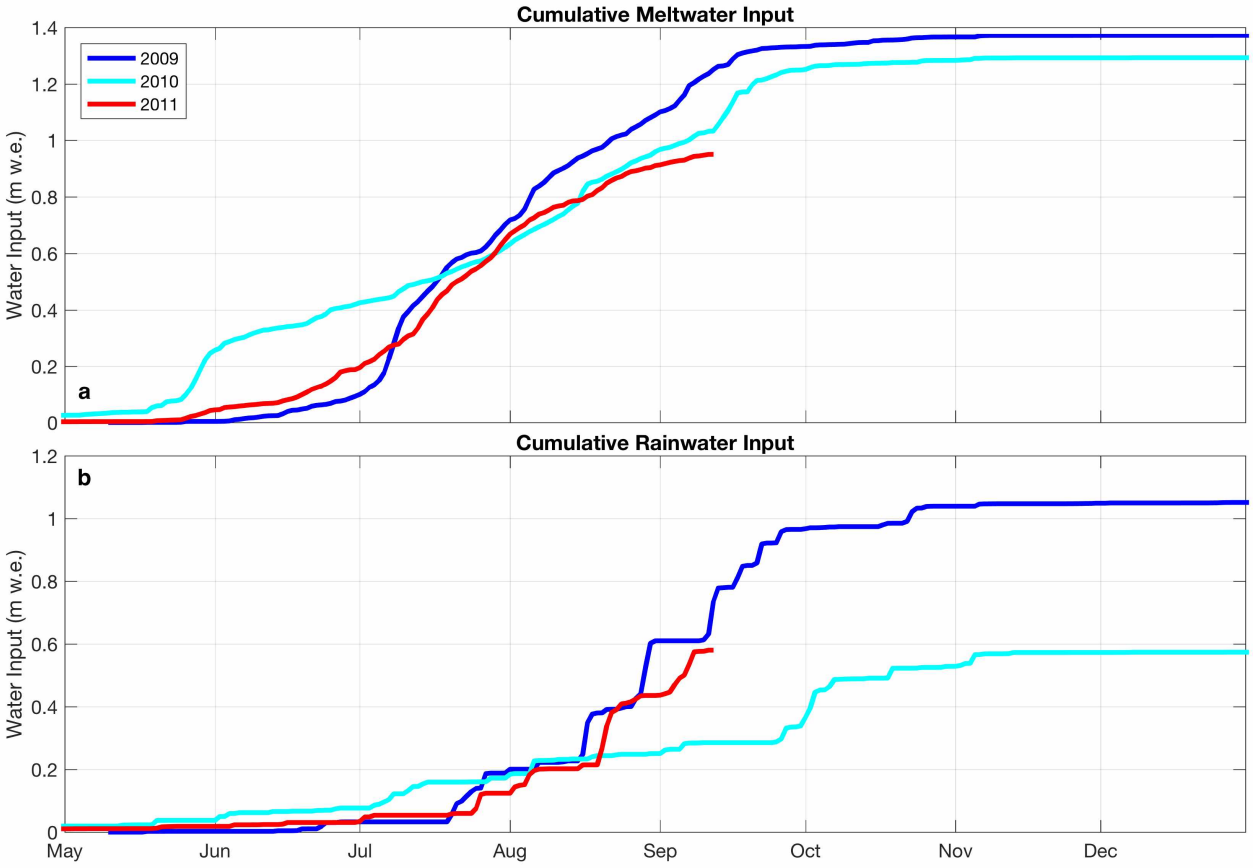

Figure 4.2. Comparison of Annual Cumulative Water Input. Cumulative annual meltwater input in meters water equivalent (m w.e.) is shown for 2009 (blue), 2010 (cyan), and 2011 (red) with respect to the day of the year. (b) Cumulative annual rainwater input for 2009–2011. (c) Cumulative annual total water input (meltwater input plus rainwater input) for 2009–2011 with the colors corresponding to the legend in (a).

4.2 Speed-Up Events

The short timescales (3–14 days) associated with the 22 observed speed-up events suggests that the observed velocity variations are mainly caused by changes in basal motion and not internal ice deformation. Each speed-up event was preceded by increased water input to the glacier's drainage system by an average of one day. This indicates variations in basal motion are a consequence of changing basal conditions triggered by increased water input.

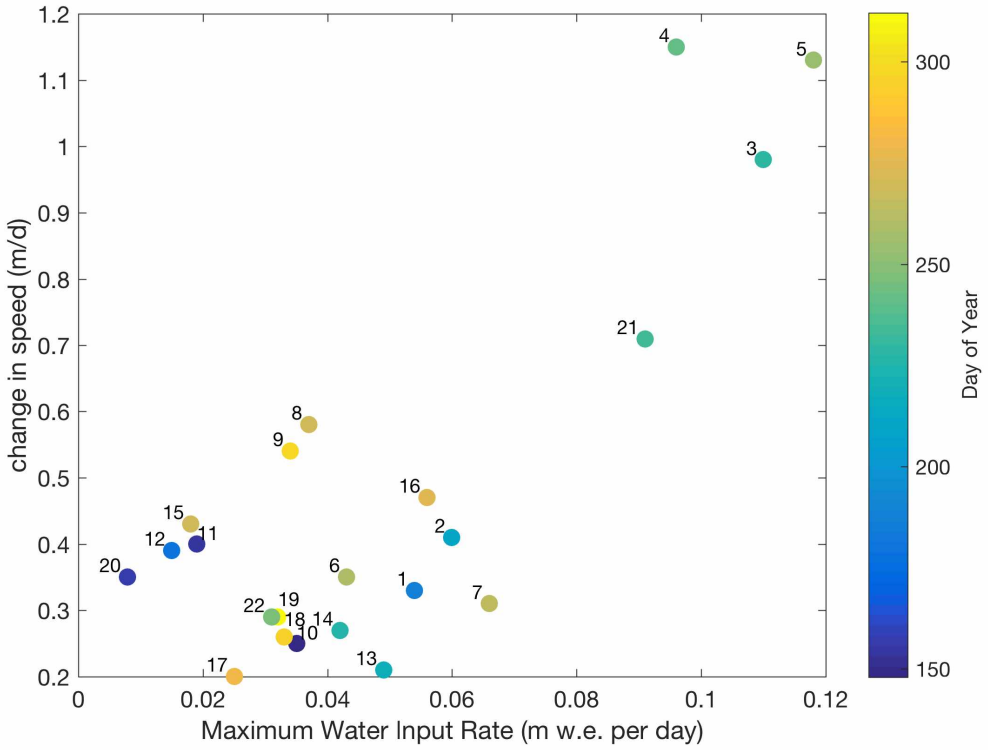

Figure 4.3. Speed-up Event and Water Input Rate Correlation. The change in velocity from before the speed-up event to the peak speed reached during the speed-up event, ($v_{peak} - v_{prior}$), in m d^{-1} is plotted against the peak water input rate in meters water equivalent per day. The color corresponds to the day of year of the peak velocity reached during each speed-up event. Day of year 150 corresponds to 30 May, 200 with 19 July, 250 with 8 September, and 300 with 27 October. The numbers correspond the name of the speed-up events, 1–9 were observed in 2009, 10–19 were observed in 2010, and 20–22 were observed in 2011

Our observations of the magnitude and timing of speed-up events indicate ice velocity is controlled by the rate and duration of water input as well as the state of the subglacial drainage system. Observations of speed-up events on Leverett Glacier in Greenland suggest that both the duration and rate of water input rather than the absolute volume were important controls on ice velocity (Bartholomew et al., 2012). The correlation between the change in velocity and maximum daily water input is shown in Figure 4.3. The velocity increase in reaching the peak velocity of the speed-up event is plotted against the peak water input rate, the colors of the points represent the day of year the peak velocity was reached during each speed-up event. This figure shows a relationship between the magnitude of the speed-up event and rate of water input. We also see that the four speed-up events with the highest magnitude are also closely related in time in the middle of the melt-season. Each speed-up event is associated with increased water inputs with durations ranging from 1–14 days. The speed-up events coupled with extra slowdowns are triggered by increased water input with durations ranging from three to four days with the exception of SE20 that was triggered by increased water inputs lasting only one day.

In addition to the rate of water inputs being a controlling factor in the magnitude of the speed-up event produced, we observe an additional correlation with time. Bartholomaus and others (2011) observed the sensitivity of sliding to daily melt water input on Kennicott Glacier changed throughout the season. They concluded that it was the state of the drainage system that determined the sensitivity of basal sliding to water inputs. Our observations of speed-up events triggered by enhanced water input also suggest that the efficiency of the drainage system impacts basal motion during the speed-up events.

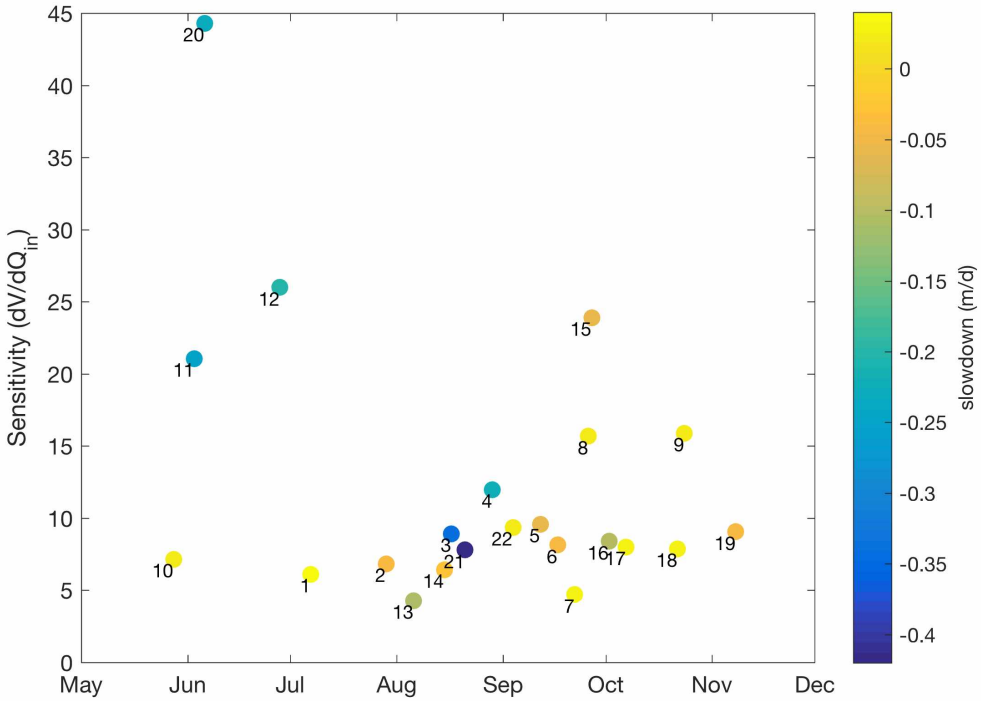

Figure 4.4. Speed-up Event Sensitivity. The sensitivity of the glacier to water inputs is estimated by dividing the maximum velocity reached during each speed-up event by the maximum water input rate corresponding to that event. This sensitivity estimate is plotted with respect to the day of year of each event. The colors correspond to the velocity decrease following the speed-up event (i.e. extra slowdown). The numbers correspond to the speed-up event names (e.g. SE1).

We observe a greater sensitivity to water input at the beginning of the melt-season and at the end of the melt-season after the onset of the winter speed-up. We compare the sensitivity of the glacier to water input to the day of year by approximating sensitivity as the maximum water input rate divided by the velocity increase, shown in Figure 4.4. The numbers correspond to the name of the speed-up events and the colors correspond to the slowdown following each speed-up event. SE4, SE13, and SE21 mark the end of the summer slowdown in 2009–2011. The winter speed-up began closely following SE8 in 2009 and SE15 in 2010. A general trend of elevated sensitivity at the beginning of the melt-season and the end of the melt-season can be seen in Figure 4.4.

4.3 Extra Slowdowns

Mid-summer heavy rainfall triggers extra slowdowns that exert the greatest control on annual average flow speeds. The peak velocity reached during the speed-up events coupled with extra slowdowns is coincident with maximum glacier wide storage and the most rapid cavity growth. The extra slowdowns are also associated with the lowering of the ice surface. These observations indicate the extra slowdowns are associated with the release of water in storage as previously isolated cavities connect and then drain into the subglacial drainage system. The resulting extra slowdowns are a consequence of increased contact between the glacier and the bed and the reduction of water pressure in the newly expanded isolated cavities.

4.3.1 Extra Slowdowns and Storage

Kamb and others (1994) observed speed-up events with extra slowdowns on Columbia Glacier, AK and recognized that surface ice velocities peaked halfway between the highest water input and discharge rates. The time difference between the water input and water output peaks is an expression of the extra storage of water englacially or subglacially during the time of each speed-up event. Water storage is defined as the time integral of the difference between water input and output rates (Kamb et al., 1994) and should peak midway in time between the input and output peaks. The timing of the speed-up events coupled with the largest extra slowdowns (SE3, SE4, and SE21) are coincident with peak water storage.

The timing of peak water input, ice velocity, and tremor amplitude for SE3–5 are shown in Figure 4.5. The first extra slowdown observed is coupled with SE3. During SE3 ice velocities increased by 55%, reaching this peak 1.5 days after peak water input. Peak tremor amplitude was reached 1.5 days after the peak ice velocity was reached, at this time ice ice velocities continued to decrease until reaching a velocity 19% lower than prior to the speed-up event. The second and final extra slowdown of 2009 was coupled with SE4. The peak surface ice velocity, a 77% increase, was reached 1.2 days after peak water input and the peak tremor amplitude was reached 1.3 days after the peak surface ice velocity. Ice velocity stabilized to 15% lower than prior to the speed-up event. The peak tremor amplitude was reached halfway between peak water input and peak tremor amplitude during both speed-up events.

The next successive speed-up event, SE5, was not coupled with an extra slowdown. SE5 did not exhibit the same timing as the two previous speed-up events despite being of a similar magnitude and followed SE4 by only eight days. The peak surface ice velocity, an 84% increase, was reached 1.1 days after peak water input and the peak tremor amplitude was reached 0.4 days after the peak velocity. The peak ice velocity did not occur approximately halfway between peak water input and peak tremor amplitude as it did for SE3 and SE4. This illustrates the peak ice velocity

being reached halfway between peak water input and output (tremor amplitude) is not the case for every speed-up event.

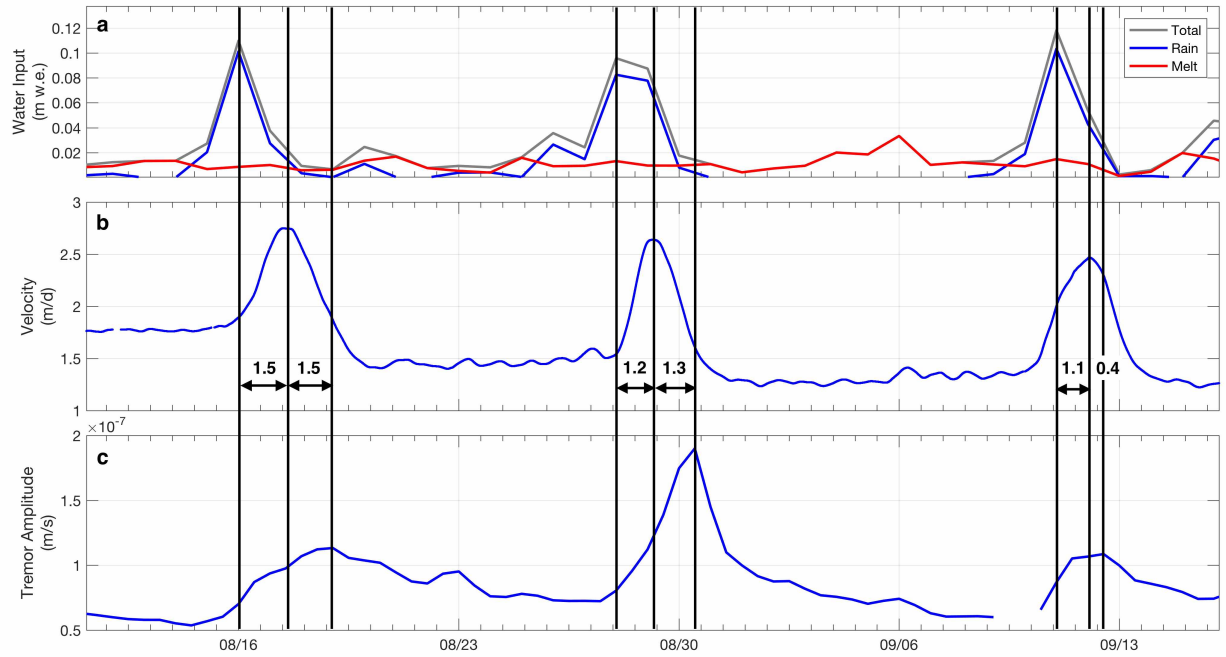

Figure 4.5. (a) Daily total water input in gray (mm w.e.), the contribution of water input from rain is shown in blue and melt is shown in red. (b) Surface ice velocity (m d^{-1}) from station CNTR for SE3–5. (c) Tremor amplitude (m s^{-1}) measured on seismic station LUPN. Black vertical lines run through peak water input, peak velocity, and peak tremor amplitude for SE3–5, the arrows and numbers refer to the time difference between the corresponding vertical lines.

The timing of peak water input, ice velocity, and tremor amplitude for SE21 in 2011, the largest extra slowdown observed, a 23% decrease, is shown in Figure 4.6. The peak ice velocity, an increase of 38%, was reached 1.2 days after peak water input. The peak tremor amplitude was reached 1.3 days after peak ice velocity. During this speed-up event the peak ice velocity was reached approximately halfway between peak water input and peak tremor amplitude.

Each of the five observed speed-up events and extra slowdowns on Yahtse have peak speeds between the highest water input rates and highest tremor amplitude, our proxy for water output (Figures 4.5 and 4.6). This suggests that ice velocities during the speed-up events coupled with extra slowdowns are controlled by the increasing volume of water in storage rater than by water input or output. If the volume of water in storage is controlling surface ice velocities during these five speed-up events we expect it would likewise control ice velocities during the associated extra slowdowns.

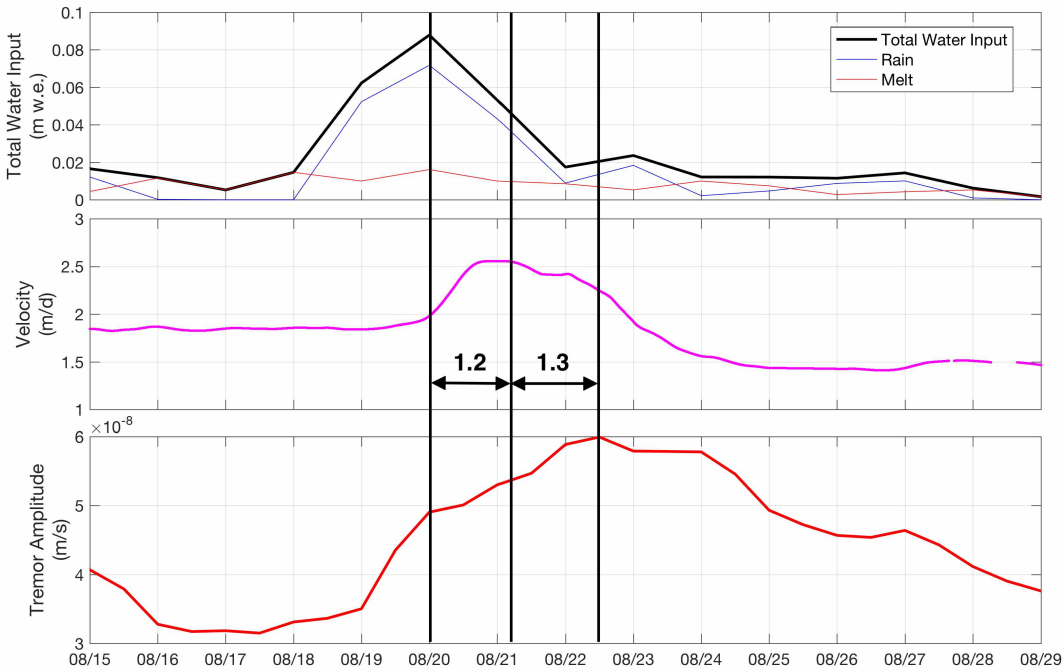

Figure 4.6. SE21 Timing. (a) Daily total water input meters water equivalent (m w.e.) where the total water input is in gray and the contribution from rain is in blue and the contribution from melt is in red. The dates refer to the 2011 melt-season. (b) Horizontal surface ice velocity (m d^{-1}) from station ONE. (c) Tremor amplitude (m s^{-1}) measured on seismic station BOOM. The solid black vertical lines are positioned at the time of maximum water input rate, maximum horizontal velocity, and maximum tremor amplitude. The double headed arrows and numbers indicate the time in days between peak water input and peak velocity and peak velocity and peak tremor amplitude.

4.3.2 Extra Slowdowns and the Isolated Cavity System

The vertical component of the GPS position data during the 2009 melt-season shows surface uplift corresponding with SE3–5 and surface lowering associated with SE3 and SE4. The surface lowering associated with the speed-up events is most easily seen on the vertical GPS data time-series detrended with respect to a fourth order polynomial fit. The raw vertical position data from station CNTR is plotted against distance along-flow and is shown in Figure 4.7a.

The vertical position data (Figure 4.7c) shows uplift of 13.7 cm associated with SE3. After the maximum uplift was reached the surface subsided, reaching a neutral position after seven days. At this time the ice surface continued lowering until the onset of SE4 on 29 August 2009, lowering a total of 3.8 cm. The surface began to rise, uplifting 5.2 cm on 30 August 2009, during SE4. After the maximum uplift was reached the ice surface began lowering, reaching a neutral position after six days. The surface continued to lower until the onset of SE5, lowering a total of 6.1 cm from before the event. Once the surface reached this height water input corresponding with SE5 caused

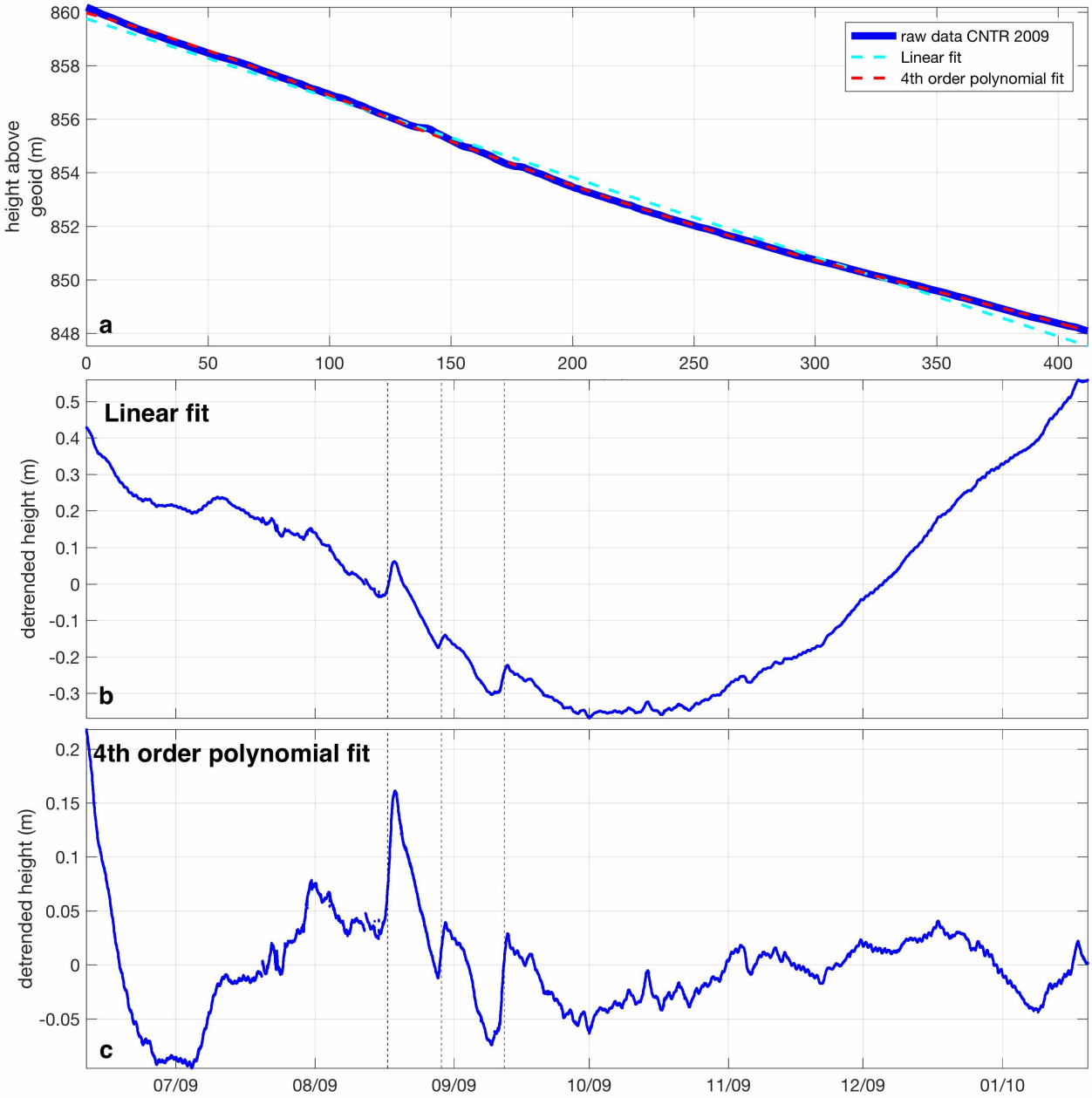

Figure 4.7. 2009 Uplift Timeseries. (a) Smoothed GPS vertical data for station CNTR (blue) plotted against the distance along-flow (m), the dashed cyan line is a linear fit and the dashed red line is a fourth degree polynomial fit. (b) The smoothed GPS vertical data less the linear line of best fit plotted against time. (c) The smoothed GPS vertical data less the 4th order polynomial line of best fit plotted against time. The dashed vertical lines correspond to the time peak velocity was reached during SE3–5.

the surface to rise again. SE5 was followed by three short periods of rainfall, ending on 1 October 2009, also the start of the winter speed-up, where the surface returned to within one centimeter of the height achieved after SE4.

The surface lowering associated with SE3 and SE4 indicates the release of water in storage at the bed of the glacier. Large volumes of water input, as was observed with SE3–5, have the ability to over pressurize the subglacial drainage system and force new pathways that connect and drain previously isolated cavities into the subglacial drainage system (Iken et al., 1983). The growth of cavities during a speed-up event increases the likelihood that they will connect and drain into the subglacial drainage system. Extra slowdowns have been shown to quantitatively correlate with significant net loss of stored water (Fahnestock, 1991). The existence of this correlation has been supported by observations of numerous glaciers (e.g. Meier et al., 1994; Kamb et al., 1994; Sole et al., 2011).

The relationship between horizontal velocity, uplift, and the rate of uplift are shown in Figure 4.8 for speed-up events 3–5 of 2009. The peak horizontal velocity during each speed-up event occurs while the glacier is rising, not when the maximum uplift (i.e. water storage) is reached. During SE3–5 the peak horizontal velocity reached is coincident with peak vertical velocity which is the time of the most rapid cavity growth (Iken et al., 1981).

The maximum velocity reached during the speed-up events coupled with extra slowdowns is coincident with the most rapid cavity growth before maximum storage is achieved. The connection of previously isolated cavities to the subglacial drainage system results in a drop in water pressure and a reduction in basal motion. While cavities that remain isolated grow as a result of the increased basal motion water pressure decreases, the volume of water within the cavities remains constant. This decreased water pressure within the isolated cavities causes them to act like "sticky spots" that impede basal motion (Iken and Truffer, 1997). Observations of Sermeq Avannarleq have indicated that the summer minimum ice velocities are controlled by the negative feedback between ice velocity and decreased water pressure in the isolated regions of the bed (Andrews et al., 2014).

Iken and Truffer (1997) proposed that when isolated cavities become interconnected there will be an increase in the amplitude of seasonal velocity variations. This is observed in our velocity record. Yahtse reached the same winter maximum velocity in 2009 and 2010. The extent of the summer slowdowns differed between years with a lower velocity reached in 2009 and 2011. The lower summer ice velocities result in a greater range of flow speeds and therefore a higher amplitude variation. Higher amplitude seasonal velocity variations were observed in both 2009 and 2011, suggesting a greater connection of cavities to the drainage system than in 2010.

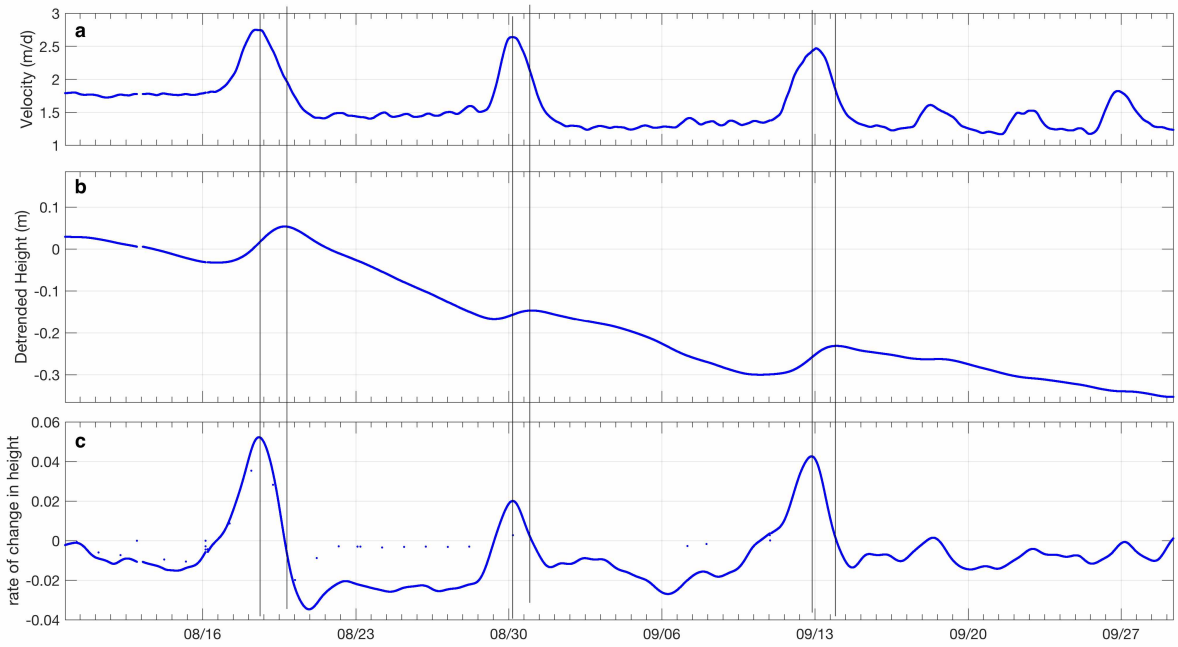

Figure 4.8. Comparison Between Uplift and Uplift Rate for SE3–5. (a) Horizontal surface ice velocity (m d^{-1}) from station CNTR for speed-up events 3–8 of 2009. (b) Detrended uplift (m) using a linear fit to the vertical position data with respect to distance downglacier. (c) Rate of uplift (m d^{-1}). The solid black vertical lines correspond to the times of maximum uplift and maximum uplift velocity for SE3–5.

4.4 Basal Hydrology Model

The basal hydrology model was able to reproduce the largest speed-up events but did not capture seasonal velocity variations. Applying this model to Yahtse Glacier has illustrated the need for an accurate Q_{in} to reproduce the magnitude of speed-up events and the need to include isolated cavities in the model to reproduce the slowdowns that control seasonal velocity variations.

The model accurately reproduced the timing and duration of the largest speed-up events but not the magnitude. This model is forced by Q_{in}, the 24-hour averaged water input rate, the magnitude of the velocity variations mirrored the magnitude of Q_{in}. This is realistic however our value for Q_{in} has large errors because of the degree day factor and lapse rate used in the water input calculations. These simplifications result in the overestimation of melt early in the melt-season and the underestimation late in the season, as well as the underestimation of rainfall as the snow/rain transition is set to mean daily values. The impact of the overestimation of meltwater input rates is best seen with SE1 (Figure 3.3) where the model produces a 98% increase in velocity but we only observe a 16% increase. Therefore the ability of the model to most accurately reproduce the magnitude of speed-up events is dependent upon the accuracy of Q_{in}.

As opposed to the findings of Brinkerhoff and others (2016) who found the model reproduced long timescale velocity variations on Kennicott well, Yahtse's long timescale velocity variability is controlled by discrete extra-slowdown events that are not reproduced. Our observations indicate isolated cavities in the subglacial drainage network are responsible for the amplitude of seasonal velocity variations (Iken and Truffer, 1997). The model assumes the connection of the subglacial drainage system and does not take into consideration the potential of isolated cavities which have been shown to both dampen velocity changes and increase the amplitude of seasonal velocity variations (Iken and Truffer, 1997).

The model does produce peaks in surface velocity during times of maximum water pressure and the fastest cavity growth which we also observe in our uplift record Figure 4.8. The timing of the velocity variations indicate that the release of water in storage as well as cavity growth is responsible for the extra slowdowns following SE3, SE4, and SE21. Water pressure within the isolated cavities decreases as cavity volume expands or as subglacial sediments deform during rapid basal sliding which can act to limit sliding (Iken and Truffer, 1997; Hoffman and Prince, 2014; Dow et al., 2013; Walter et al., 2014).

With an accurate Q_{in} that will more accurately reproduce the magnitudes of the speed-up events and the inclusion of isolated cavities the model should be able to reproduce the observed extra-slowdown events that control seasonal velocity variations.

Chapter 5
Conclusion

High rates of water input to the bed trigger the speed-up events that modulate melt-season behavior. The high water input rates associated with heavy rainfall over several days can lower summer ice speeds enough to lower average annual speeds. The summer minimum speed impacts ice flow until mid-winter, after which ice flow returns to pre-melt-season levels. Therefore, late-summer heavy rainfall exerts the strongest control on annual average ice velocities.

In the introduction we posed a number of research questions that we can now answer:

- How much does water input contribute to the velocity variations observed on Yahtse?
  Water inputs trigger all speed-up events observed on Yahtse Glacier. However, it is the state of the subglacial drainage system that governs the magnitude of the speed-up event.

- Does the glacier's response to water input change over time?
  Yahtse is most sensitive to water inputs when the englacial and subglacial drainage systems are least efficient. We observe higher sensitivity at the beginning of the melt-season and after the onset of winter speed-up when the well established drainage systems begins to close.

- Does the glacier exhibit the same ice velocities from year to year?
  Yahtse exhibits a seasonal pattern of a summer slowdown superimposed with speed-up events and extra slowdowns, the extent of which is determined by discrete periods of heavy rainfall. After the minimum speeds are reached speed-up events no longer slowdown the glacier. These minimum speeds are maintained until October when a winter speed-up begins. Pre-melt-season speeds are reached in January and maintained until the onset of melt.

- Is the winter velocity inversely related to meltwater input (Burgess et al., 2013a)?
  We found a relationship between lower winter ice velocities and heavy rainfall over several days in mid-August and early-September. These discrete periods of high water input rates trigger extra slowdowns that release water from storage and further develop the channelized subglacial drainage system, resulting in lower summer ice velocities. The summer minimum ice velocity impacts flow speeds until mid-winter.

- Can we predict the ice velocities based on the velocity record from the previous year? Each melt-season begins with similar ice velocities that are reached in mid-winter and maintained until the onset of melt. This indicates that the subglacial drainage system is dominated by isolated and linked-cavities at the beginning of each melt-season regardless of the extent of channelization reached the previous year. Therefore the efficiency reached during one year will not impact the state of the subglacial drainage system at the beginning of the next melt-season.

In conclusion, our data suggest that the presence of mid-summer heavy rainfall events lowers annual average ice velocities. Our model demonstrates the need for the inclusion of the isolated cavity system in the basal hydrology model to reproduce the triggered extra slowdowns that control the summer slowdown and to model the winter speed-up. While high rates of rainfall produce speed-up events, their ability to connect isolated subglacial cavities has a greater impact on annual ice velocities and therefore the ice discharged at the terminus. Therefore it is short lived heavy rainfall rather than meltwater input that exerts the greatest control on annual ice velocities and therefore ice discharge at the terminus.

Chapter 6

References

Ambach, W. (1988). Interpretation of the positive-degree-days factor by heat balance characteristics–West Greenland. Hydrology Research, 19(4), 217–224.

Anderson, R. S., Anderson, S. P., MacGregor, K. R., Waddington, E. D., O'Neel, S., Riihimaki, C. A., & Loso, M. G. (2004). Strong feedbacks between hydrology and a sliding of a small alpine glacier. Journal of Geophysical Research: Earth Surface, 109(F3).

Andrews, L. C., Catania, G. A., Hoffman, M. J., Gulley, J. D., Lüthi, M. P., Ryser, C., Hawley, R. L., & Neumann, T. A. (2014). Direct observations of evolving subglacial drainage beneath the Greenland Ice Sheet. Nature, 514(7520), 80–83.

Barclay, D. J., Wiles, G. C., & Calkin, P. E. (2009). Holocene glacier fluctuations in Alaska. Quaternary Science Reviews, 28(21), 2034–2048.

Bartholomaus, T. C., Anderson, R. S., & Anderson, S. P. (2007). Response of glacier basal motion to transient water storage. Nature Geoscience, 1(1), 33–37.

Bartholomaus, T. C., Anderson, R. S., & Anderson, S. P. (2011). Growth and collapse of the distributed subglacial hydrologic system of Kennicott Glacier, Alaska, USA,and its effects on basal motion. Journal of Glaciology, 57(206), 985–1002.

Bartholomaus, T. C., Larsen, C. F., O'Neel, S., & West, M. E. (2012). Calving seismicity from iceberg sea surface interactions. Journal of Geophysical Research: Earth Surface, 117(F4).

Bartholomaus, T. C. (2014) Seismicity, seawater and seasonality: new insights into iceberg calving from Yahtse Glacier, Alaska. (Doctoral Dissertation University of Alaska Fairbanks).

Bartholomaus, T. C., Amundson, J. M., Walter, J. I., O'Neel, S., West, M. E., & Larsen, C. F. (2015). Subglacial discharge at tidewater glaciers revealed by seismic tremor. Geophysical Research Letters, 42, 6391–6398.

Bartholomew, I., Nienow, P., Sole, A., Mair, D., Cowton, T., & King, M. (2012). Short-term variability in Greenland Ice Sheet motion forced by time-varying meltwater drainage: Implications for the relationship between subglacial drainage system behavior and ice velocity. Journal of Geophysical Research, 117(F03002), 1–17.

Bindschadler, R. (1983). The importance of pressurized subglacial water in separation and sliding at the glacier bed. Journal of Glaciology, 29(101), 3–19.

Braithwaite, R. J., & Olesen, O. B. (1990). A simple energy-balance model to calculate ice ablation at the margin of the Greenland ice sheet. Journal of Glaciology, 36(123), 222–228.

Braithwaite, R. J. (1995). Aerodynamic stability and turbulent sensible-heat flux over a melting ice surface, the Greenland ice sheet. Journal of Glaciology, 41(139), 562–571.

Brinkerhoff, D. J., Meyer, C. R., Bueler, E., Truffer, M., & Bartholomaus, T. C. (2016). Inversion of a glacier hydrology model. Annals of Glaciology, 57(72), 1–12.

Burgess, E. W., Larsen, C. F., & Forster, R. R. (2013a). Summer melt regulates winter glacier flow speeds throughout Alaska. Geophysical Research Letters, 40, 6160–6164.

Burgess, E. W., Forster, R. R., & Larsen, C. F. (2013b). Flow velocities of Alaska glaciers. Nature Communications, 4.

Copland, L., Sharp, M. J., Nienow, P. W. (2003). Links between short-term velocity variations and the subglacial hydrology of a predominantly cold polythermal glacier. Journal of Glaciology, 49(166), 337–348.

Dow, C. F., Hubbard, A., Booth, A. D., Doyle, S. H., Gusmeroli, A. & Kulessa, B. (2013). Seismic evidence of mechanically weak sediments underlying Russell Glacier, West Greenland, Annals of Glaciology, 54(64), 135–141.

Fahnestock, M. A. (1991). Hydrologic control of sliding velocity in two Alaskan glaciers: observation and theory (Doctoral dissertation, California Institute of Technology).

Fountain, A. G., & Walder, J. S. (1998). Water flow through temperate glaciers. Reviews of Geophysics, 36(97), 299–328.

Gimbert, F., Tsai, V. C., Amundson, J. M., Bartholomaus, T. C., & Walter, J. I. (2016). Subseasonal changes observed in subglacial channel pressure, size, and sediment transport. Geophysical Research Letters, 43(8), 3786–3794.

Gudmundsson, G. H., Bassi, A., Vonmoos, M., Bauder, A., Fischer, U. H., & Funk, M. (2000). High-resolution measurements of spatial and temporal variations in surface velocities of Unteraargletscher, Bernese Alps, Switzerland. Annals of Glaciology, 31(1), 63–68.

Hairer, E., Norsett, S. P., & Wanner, G. (1993). Solving Ordinary Differential Equations I. Non-stiff Problems. 2nd edition. Springer Series in Computational Mathematics, Springer-Verlag (1993).

Hock, R. (2003). Temperature index melt modelling in mountain areas. Journal of Hydrology, 282(1), 104–115.

Hodge, S. M. (1974). Variations in the sliding of a temperate glacier. Journal of Glaciology, 13(69), 349–369.

Hoffman, M., & Prince, S. (2014). Feedbacks between coupled subglacial hydrology and glacier dynamics. Journal of Geophysical Research: Earth Surface, 119, 414–436.

Howat, I. M., Tulaczyk, S., Waddington, E., & Björnsson, H. (2008). Dynamic controls on glacier basal motion inferred from surface ice motion. Journal of Geophysical Research: Earth Surface, 113(F3).

Hubbard, B., & Nienow, P. (1997). Alpine subglacial hydrology. Quaternary Science Reviews, 16(9), 939–955.

Iken, A. (1981). The effect of the subglacial water pressure on the sliding velocity of a glacier in an idealized numerical model. Journal of Glaciology, 27(97),407–421.

Iken, A., Röthlisberger, H., Flotron, A., & Haeberli, W. (1983). The uplift of Unteraargletscher at the beginning of the melt season–a consequence of water storage at the bed? Journal of Glaciology, 29(101), 28–47.

Iken, A., & Bindschadler, R. A. (1986). Combined measurements of subglacial water pressure and surface velocity of Findelengletscher, Switzerland: conclusions about drainage system and sliding mechanism. Journal of Glaciology, 32(110), 101–119.

Iken, A., & Truffer, M. (1997). The relationship between subglacial water pressure and velocity of Findelengletscher, Switzerland, during its advance and retreat. Journal of Glaciology, 43(144), 328–338.

Jansson, P. (1995). Water pressure and basal sliding on Storglaciären, northern Sweden. Journal of Glaciology, 41(138), 232–240.

Kamb, B. & Echelmeyer, K. A. (1986). Stress-gradient coupling in glacier flow: I. Longitudinal averaging of the influence of ice thickness and surface slope. Journal of Glaciology, 32(111), 267–284.

Kamb, B. (1987). Glacier surge mechanism based on linked cavity configuration of the basal water conduit system. Journal of Geophysical Research: Solid Earth, 92(B9), 9083–9100.

Kamb, B., Engelhardt, H., Fahnestock, M. A., Humphrey, N., Meier, M., & Stone, D. (1994). Mechanical and hydrologic basis for the rapid motion of a large tidewater glacier: 2. Interpretation. Journal of Geophysical Research: Solid Earth, 99(B8), 1523–5244.

Kessler, M. A., & Anderson, R. S. (2004). Testing a numerical glacial hydrological model using spring speed-up events and outburst floods. Geophysical Research Letters, 31(18).

Lang, H., & Braun, L. (1990). On the information content of air temperature in the context of snow melt estimation. IAHS Publ, 190, 347–354.

Larsen, C., & West, M. (2009): Collaborative Research: Relating glacier-generated seismicity to ice motion, basal processes and iceberg calving. International Federation of Digital Seismograph Networks. Seismic Network. doi:10.7914/SN/XF_2009.

Lliboutry, L. (1979). Local friction laws for glaciers: a critical review and new openings. Journal of Glaciology, 7(49), 21–58.

McNamara, D. E., & Buland, R. P. (2004). Ambient noise levels in the continental United States, Bulletin Seismological Society of America, 94(4), 1517–1527.

Meier, M., & Post, A. (1987). Fast Tidewater Glaciers, Journal of Geophysical Research, 92(B9), 9051–9058.

Meier, M., Lundstrom, S., Stone, D., Kamb, B., Engelhardt, H., Humphrey, N., & Walters, R. (1994). Mechanical and hydrologic basis for the rapid motion of a large tidewater glacier: 1. Observations. Journal of Geophysical Research: Solid Earth (1978–2012), 99(B8), 15219–15229.

Menne, M. J., Durre, I., Vose, R. S., Gleason, B. E., & Houston, T. G. (2012). An overview of the Global Historical Climatology Network-Daily Database. Journal of Atmospheric and Oceanic Technology, 29, 897–910.

Menne, M. J., Durre, I., Korzeniewski, B., McNeal, S., Thomas, K., Yin, X., Anthony, S. Ray, R., Vose, R. S., Gleason, B. E., & Houston, T. G. (2012). Global Historical Climatology Network - Daily (GHCN-Daily), Version 3. [GHCND:USW00025339 - Yakutat Airport, AK US]. NOAA National Climatic Data Center. doi:10.7289/V5D21VHZ [28 October 2015]

Moschas, F., & Stiros, S. (2013). Noise characteristics of high-frequency, short-duration GPS records from analysis of identical, collocated instruments. Measurement, 46(4), 1488–1506.

Munson, B. R., Young, D. F., & Okiishi, T. H. (2005). Fundamentals of fluid mechanics, 5th edition. Wiley, Hoboken, NJ.

Natural Resources Canada (2016). Canadian Geodetic Survey - Canadian Spatial Reference System-Precise Point Positioning Online Tool (Version v1.4) [Web application software]. Retrieved from `https://webapp.geod.nrcan.gc.ca/geod/tools-outils/ppp.php`

Nye, J. F. (1976). Water flow in glaciers: jökulhlaups, tunnels & veins. Journal of Glaciology, 17(76), 181–207.

Ohmura, A. (2001). Physical basis for the temperature-based melt-index method. Journal of Applied Meteorology, 40(4), 753–761.

O'Neel, S., Pfeffer, T. W., Krimmel, R., & Meier, M. (2005). Evolving force balance at Columbia Glacier, Alaska, during its rapid retreat. Journal of Geophysical Research, 110(3), 1–18.

Podrasky, D., Truffer, M., Fahnestock, M., Amundson, J. M., Cassotto, R., & Joughin, I. (2012). Outlet glacier response to forcing over hourly to inter-annual timescales, Jakobshavn Isberæ, Greenland. Journal of Glaciology, 58(212), 1212–1226.

Post, A., & Mayo, L. R. (1971). Glacier dammed lakes and outburst floods in Alaska (p. 10). Washington: US Geological Survey.

Press, W. H. , Flannery, B. P., Teukolsky, S. A., & Vetterling, W. T. (1988). Numerical Recipes in C: The Art of Scientific Computing, 1st ed. Cambridge University Press, Cambridge, U.K.

Raymond, C. F., Benedict, R. J., Harrison, W. D., Echelmeyer, K. A., & Sturm, M. (1995). Hydrological discharges and motion of Fels and Black Rapids Glaciers, Alaska, U.S.A.: implications for the structure of their drainage systems. Journal of Glaciology, 41(138), 290–304.

Rignot, E. & Kanagaratnam, P. (2006). Changes in the velocity of the Greenland Ice Sheet. Science, 311, 986–990.

Roe, G. H. (2005). Orographic precipitation. Annual Reviews Earth and Planetary Sciences, 33, 645–671.

Röthlisberger, H. (1972). Water pressure in intra-and subglacial channels. Journal of Glaciology, 11(62), 177–203.

Sato, A., Takahashi, S., Naruse, R., & Wakahama, G., (1984). Ablation and heat balance of the Yukikabe snow patch in the Daisetsu mountains. Annals of Glaciology, 5, 122–126.

Schoof, C. (2010). Ice sheet acceleration driven by melt supply variability. Nature, 468(7325), 803–806.

Schoof, C., Hewitt, I. J., & Werder, M. A. (2012). Flotation and free surface flow in a model for subglacial drainage. Part 1. Distributed drainage. Journal of Fluid Mechanics, 702, 126–156.

Sole, A. J., Mair, D. W. F., Nienow, P. W., Bartholomew, I. D., King, M. A., Burke, M. J., & Joughin, I. (2011). Seasonal speedup of a Greenland marine terminating outlet glacier forced by surface melt-induced changes in subglacial hydrology. Journal of Geophysical Research: Earth Surface, 116(F3).

Sugiyama, S., & Gudmundsson, G. (2003). Diurnal variations in vertical strain observed in a Temperate valley glacier. Geophysical Research Letters, 30(2), 3–6.

Sundal, A.V., Shepherd, A., Nienow, O., Hanna, E., Palmer, S., & Huybrechts, P., (2011). Melt-induced speed-up of Greenland ice sheet offset by efficient subglacial drainage. Nature, 469, 521–524

Truffer, M., Echelmeyer, K. A., & Harrison, W. D. (2001). Implications of till deformation on glacier dynamics. Journal of Glaciology, 47(156), 123–134.

van den Broeke, M. R. (1997). Momentum, heat, and moisture budgets of the katabatic wind laye over a midlatitude glacier in summer. Journal of Applied Meteorology, 36(6), 763–774.

Vieli, A., Jania, J., Blatter, H., & Funk, M. (2004). Short-term velocity variations on Hansbreen, a tidewater glacier in Spitsbergen. Journal of Glaciology, 50(170), 389–398.

Walder, J. S. (1986). Hydraulics of subglacial cavities. Journal of Glaciology, 32(112), 439–445.

Walter, F., Chaput, J., & Lüthi, M. P. (2014). Thick sediments beneath Greenland's ablation zone and their potential role in future ice sheet dynamics. Geology, 42(6), 487–490.

Weertman, J. (1964). The theory of glacier sliding. Journal of Glaciology, 5(39), 287–303.

Western Regional Climate Center. (2015). Bering Glacier Alaska Data Inventory. Retrieved from `http://www.wrcc.dri.edu/cgi-bin/rawMAIN.pl?akABER`

Willis, I. C. (1995). Intra-annual variations in glacier motion: a review. Progress in Physical Geography, 19(1), 61–106.

Wyatt, F. R., & Sharp, M. J. (2015). Linking surface hydrology to flow regimes and patterns of velocity variability on Devon Ice Cap, Nunavut. Journal of Glaciology, 61(226), 387–399.

Zwally, H.J., W. Abdalati, T. Herring, K. Larson, J.S., & K. Steffen (2002). Surface melt-induced acceleration of Greenland ice-sheet flow. Science, 297(5579), 218–222.